Complex Rab4-mediated regulation of endosomal size and EGFR activation

Kate Tubbesing[1], **Jamie Ward**[1], **Ray Abini-Agbomson**[1], **Aditi Malhotra**[1], **Alena Rudkouskaya**[1], **Janine Warren**[1], **John Lamar**[1], **Nina Martino**[1], **Alejandro P. Adam**[1,2], **Margarida Barroso**[1]

[1]Department of Molecular and Cellular Physiology, Albany Medical College, Albany, NY

[2]Department of Ophthalmology, Albany Medical College, Albany, NY

Abstract

Early sorting endosomes are responsible for the trafficking and function of transferrin receptor (TfR) and epidermal growth factor receptor (EGFR). These receptors play important roles in iron uptake and signaling and are critical for breast cancer development. However, the role of morphology, receptor composition, and signaling of early endosomes in breast cancer remains poorly understood. A novel population of enlarged early endosomes was identified in breast cancer cells and tumor xenografts but not in non-cancerous MCF10A cells. Quantitative analysis of endosomal morphology, cargo sorting, EGFR activation and Rab GTPase regulation was performed using super-resolution and confocal microscopy followed by 3D rendering. MDAMB231 breast cancer cells have fewer, but larger EEA1-positive early endosomes compared to MCF10A cells. Live-cell imaging indicated dysregulated cargo sorting, since EGF and Tf traffic together via enlarged endosomes in MDAMB231, but not in MCF10A. Large EEA1-positive MDAMB231 endosomes exhibited prolonged and increased EGF-induced activation of EGFR upon phosphorylation at tyrosine-1068 (EGFR-p1068). Rab4A over-expression in MCF10A cells produced EEA1-positive enlarged endosomes that displayed prolonged and amplified EGF-induced EGFR-p1068 activation. Knock-down of Rab4A lead to increased endosomal size in MCF10A but not in MDAMB231 cells. Nevertheless, Rab4A knock-down resulted in enhanced EGF-induced activation of EGFR-p1068 in MDAMB231 as well as downstream signaling in MCF10A cells. Altogether, this extensive characterization of early endosomes in breast cancer cells has identified a Rab4-modulated enlarged early endosomal compartment as the site of prolonged and increased EGFR activation.

Corresponding author: Margarida Barroso: 47 New Scotland Avenue, Albany Medical College, Albany NY 12208; Phone: 518-262-6435; barrosm@amc.edu; Twitter: @barrosolab.

INTRODUCTION

Characterization of the morphology and subcellular localization of early endosomes (EE) is essential for the understanding of receptor trafficking and signaling in cancer cells. Recently, the endocytic pathway has been shown to be defective in various human cancers (1,2). Furthermore, clathrin-dependent and -independent endocytosis show significant alterations in several cancer cell lines (3–5). Importantly, the size and cellular distribution of endosomes have been suggested as a potential biomarker in cancer (6). Moreover, perinuclear endosomal signaling complexes have been shown to play a crucial role in the regulation of signaling cascades involved in cancer progression (7). However, many aspects of EE function, regulation, and morphology in breast cancer cells remain unclear.

Membrane-bound receptors involved in nutrient uptake, e.g. transferrin-receptor (TfR) and low-density lipoprotein (LDL), as well as in cell signaling, e.g. epidermal growth factor receptor (EGFR), play an important role in cancer development and progression. These receptors are endocytosed via multiple internalization pathways into EE, which act as a literal "fork in the road", as both the endocytic recycling and lysosomal pathways are initiated from this dynamic organelle (8,9). Thus, while multiple receptors share an initial endocytosis pathway, their cellular fate can differ substantially. For example,Tf bound to its receptor delivers iron into cells via the early and recycling endocytic pathway (10), whereas LDL, which plays a key role in lipid metabolism, is released from LDLR in EE and delivered to late endosomes/lysosomes (11). Moreover, EGF-induced internalization of EGFR into EEs is required for its signaling function, and EGFR's kinase activity is downregulated via the ubiquitination-dependent late endosomal/lysosomal pathway (12). Therefore, studying the altered endocytic trafficking of Tf-TfR, EGF-EGFR, and LDL-LDLR in cancer is crucial to advance our understanding of the crosstalk between cell signaling and metabolism.

Endosomal compartments are identified and regulated by one or more small Rab-GTPases, which modulate essential membrane functions via interactions with Rab effector proteins (9,13). Rab5 is an important regulator of the EEs (9). Two well-characterized Rab5 effectors, EEA1 (EE Antigen 1) and APPL1, can occupy the same or separate EEs (14,15). Altered expression and activity levels of Rab GTPases affect the endocytosis, degradation and recycling of membrane-bound receptors, leading to increased cancer cell proliferation and motility as well as metastatic behavior (1,2,16,17).

Rab4 is the most commonly amplified Rab GTPase in invasive breast carcinoma (4). Rab4 and Rab11 work in a coordinated manner to regulate the fast and slow recycling compartments, respectively (18–20). Moreover, Rab4 was shown to influence Tf-mediated cellular iron accumulation (21). Rab4 inactivation, through expression of either a dominant-negative Rab4-S22N mutation or a Rab4 GTPase activating protein (TBC1D16), increases EGFR degradation (22,23) and weakens the invasive behavior of breast cancer cells *in vivo*

(4). As the regulation of EGFR trafficking and signaling involves multiple Rab proteins, the role of Rab4 in EGFR regulation remains unclear (24).

EEs have been characterized as tubulo-vesicular compartments with an average diameter between 100–500 nm (9,25). In this study, super-resolution (SR) microscopy, time-lapse live-cell imaging, and 3D whole-cell quantitative microscopy approaches, as well as immunostaining and immunoblotting signaling assays were used to characterize an enlarged endosomal population that is also the site of increased and prolonged EGF-induced EGFR activation upon phosphorylation at tyrosine 1068 (EGFR-p1068), in aggressive triple-negative MDAMB231 cells but not in non-transformed mammary epithelial MCF10A cells MCF10A cells. Furthermore, Rab4A over-expression lead to an increase in EEA1-positive endosomal size as well as an extended and elevated EGF-induced EGFR-p1068 activation in those enlarged endosomes in MCF10A cells. Unexpectedly, Rab4A knockdown lead to an increased endosomal size in MCF10A but not in MDAMB231 cells. Nevertheless, Rab4A-depleted MDAMB231 cells displayed an elevated EGF-induced activation of EGFR-p1068. These findings establish enlarged EEs in breast cancer cells as central players in the regulation of cargo trafficking and cell signaling, Here, we suggest a complex role for Rab4 in the regulation of endosomal size as well as of intensity and duration of EGFR activation.

MATERIAL AND METHODS

Cell culture

Cells were purchased from ATCC (Manassas, VA) and tested routinely for mycoplasma. MCF10A cells were cultured in DMEM/F12 with 5% horse serum, 20 ng/ml EGF, 0.5 mg/mL hydrocortisone, 100 ng/ml cholera toxin, 10 μg/mL bovine insulin and penicillin/streptomycin. Human breast cancer cells were cultured in DMEM with 10% fetal bovine serum (FBS), 4 mM L-glutamine and 10 mM HEPES, pH 7.4. Cells were passaged less than 15 times. No further cell line authentication was performed. For imaging, cells were plated onto poly-D-lysine coated glass-bottom dishes with №1.5 glass (Mattek, MA). Clear imaging (CI) medium consisted of phenol-free DMEM with 0.5% bovine serum albumin (BSA), 4 mM L-glutamine and 20 mM HEPES, pH 7.4. Chemicals used in solutions and kits are described in Table S1.

Plasmids, transfection and lentiviral infection

Transfections were performed by electroporation using Neon transfection system (ThermoFisher, MA) and Neon reagents with pulse-width optimized per cell line. Lentiviral particles were packaged and collected from HEK239 cells (Thermo Fisher, MA). Concentration of viral particles was performed with Vivcell100, 30 kDa concentrators (Sartorius, Germany). Immunoblots were used to confirm depletion or over-expression of Rab4. Plasmids were sequenced through Genewiz for confirmation of mutation sequences or successful cloning. Source of plasmids is described in Table S2.

Immunofluorescence, immunoblotting and antibody validation

Cells were fixed for 15 min with 4% paraformaldehyde (PFA), permeabilized with 0.1% TX-100 in PBS for 15 min and blocked for 90 min in 2% fish skin gelatin (FSG), 1% BSA

in PBS. Washing and antibody blocking were performed using 0.5% FSG, 0.05% TX-100 in PBS. Antibody validation was performed via cell transfection with target-fluorescent protein constructs, followed by immunostaining and quantitative colocalization analysis of confocal images. Pearson's correlation coefficient of 0.9 indicated a highly specific antibody. Whole cell lysates were processed for immunoblotting using standard methods (26). Antibodies are listed in Table S3. EGF binding assays are described in Supplementary Methods.

Tumor xenografts

All animal procedures were conducted with the approval of the Institutional Animal Care and Use Committee at Albany Medical College, which is AALAC accredited. Human tumor xenografts were generated as described in (27).

3D dSTORM microscopy

Cells were pre-incubated for 30 min with CI medium and incubated with 20 μg/mL AF647-Tf in CI medium for 1 h, prior to PBS washes and fixation with 4% PFA. 3D *d*STORM microscopy and post-processing image analysis was performed as described in (28) and in Supplementary Methods.

Confocal and Airyscan microscopy

Zeiss LSM880 with Fast Airyscan detector or LSM510 (Zeiss, Germany) were used to collect z-stack images. Fast Airyscan was performed at Nyquist sampling and using SR settings. For whole cell analysis, z-stack images were collected to visualize cells from top to bottom, and for live-cell imaging, 3–5 images per z-stack were collected per time point. Airyscan processing (pixel reassignment) was performed in Zen Black software under default settings. Live-cell imaging is described in Supplementary Methods.

Colocalization Analysis

Pearson's correlation coefficient in z-stacks was determined using "coloc" module from Imaris software (Bitplane Inc.). For statistical analysis, at least 3 z-stack whole images per condition were analyzed. Extended description of the colocalization analysis is found in Supplementary Methods and Figure S1.

3D rendering

The "surface" module in Imaris 8.4 software (Bitplane Inc.) was used to perform the 3D rendering of endocytic structures labeled with EEA1, Tf, LDL, EGF or EGFR as complex 3D objects (28). Smoothing and background subtraction was held constant within a given set of experiments, while thresholding settings were adjusted to provide improved 3D rendering upon visual inspection. Additional details on 3D rendering approaches are in Supplementary Methods.

Tf recycling plate-reader assay

Cells were plated on 96-well black plates with optically clear plastic bottoms. Cells were pre-cleared in CI medium for 30 min at 37°C, incubated with AF647-Tf (10 μg/mL) for 1 h, washed, and then chased with CI medium for different periods of time. Upon fixation, the

amount of labeled-Tf remaining in the cells was measured using Molecular Devices Flexstation III (Molecular Devices) and associated SoftmaxPro5 software. To address the differences in total Tf uptake between cell lines, within each recycling assay, each cell line is normalized to itself at the 0 min chase time point, following background subtraction.

Statistical analysis

The statistical significance of the data was tested with either, Two-tailed Student's t tests or Anova (single-factor or two-factor). Differences were considered significant if the p-value < 0.05. Error bars indicate 95% confidence interval. The raw statistical values of each image were exported and compiled with Excel (Office 365 ProPlus), while Origin software (Origin Lab, Northampton, MA) was utilized for graph generation and statistical analysis.

RESULTS

Early endosomal morphology is altered in breast cancer cells and tumor xenografts

Morphological studies of EEs in breast cancer cells or tumor xenografts are lacking despite their important role in cancer cells function and survival (1,3). To address this, a morphological evaluation of EE immunostained with anti-EEA1 was performed in a panel of human breast cancer cells, including T47D cells that denote estrogen receptor-positive breast cancer (27,29), and MDAMB231, MDAMB436 and MDAMB468 that represent three different types of triple-negative breast cancer cells (30,31) as well as non-cancerous mammary epithelial MCF10A cells. High-resolution confocal imaging clearly showed distinct EEA1 morphological patterns in terms of size and cellular distribution in all five cell lines (Figure 1A). MCF10A cells presented a larger number of small endosome punctate structures, evenly distributed throughout the cell. Other non-cancerous cells such as human mammary epithelial cells (HMEC) displayed a similar EE morphology to that of MCF10A cells (Figure S2). These results suggest that an endosomal morphology in which numerous small vesicles are distributed across the cell is typical of mammary epithelial cells in 2D cell culture models.

MDAMB231 cells displayed the largest endosomes with a perinuclear distribution. T47D cells also displayed endosomal structures that appear larger than those in MCF10A cells but were evenly distributed across the cell. MDAMB436 cells displayed endosomes of varying size clustered in a perinuclear pattern. MDAMB468 cells showed a strikingly small cytoplasm volume with endosomes scattered throughout the cell. The relative endosomal volume of MDAMB468 may be larger than that of normal cells when considering their smaller cell size. Moreover, the endosomal morphology was evaluated in MDAMB231 and T47D tumor xenografts using a similar imaging approach. The enlarged EEA1-positive endosomes were clearly visible in both MDAMB231 and T47D xenograft tissue sections (Figure 1B). This initial evaluation established the heterogeneity of endosomal morphologies in breast cancer, with an outstanding trend of fewer but larger EEA1-positive endosomes in cancer cells both *in vitro* and *in vivo*.

To further define the EEA1-positive EE compartment in breast cancer cells, we evaluated the presence or absence of other endosomal markers. To characterize protein co-localization on

endosomal vesicles based not on cooccurrence but functional relationships, we have calculated Pearson's correlation coefficient from a 3D data set (z-stack) using the "coloc" module from Imaris software (Bitplane Inc.) (32); a detailed justification for the use of Pearson's correlation coefficient is included in Supplementary Methods. The EEA1-positive compartment did not display significant colocalization with autophagy marker LC3, since cells were not subjected to prolonged serum starvation to avoid induction of autophagy (33) (Figure 1C & E, Figure S3). MDAMB231 showed increased cellular staining of LC3, compared to MCF10A or T47D. Following a 1 h continuous internalization, Tf is localized to both early and recycling compartments along the endosomal pathway (8). However, in contrast to EEA1, which colocalizes with intracellular Tf, LC3 showed reduced colocalization with Tf and EEA1 in all three cell lines evaluated (Figure 1E, Table S4). Arrowheads in Figure 1C indicate discrete punctate structures of varying size that display Tf and EEA1, but no LC3 staining, indicative of their early endosomal nature. Tf-positive structures, lacking EEA1 staining, may reflect localization to the endocytic recycling compartment. The reduced colocalization of Tf with EEA1 in MCF10A cells could indicate a shift of Tf to a recycling compartment at this time-point, and/or be a result of reduced Tf uptake compared to MDAMB231 and T47D cells (Figure 1E). Furthermore, EEA1 was found to be highly colocalized with AP3 In MCF10A and MDAMB231 cells (Figure 1D & F). AP3 is an adaptor protein, which regulates transport of receptors via endocytic budding events (with and without clathrin), and is predominantly associated with EEs (34,35).

The protein expression and localization of Rab-GTPases is known to regulate the early, recycling and late endocytic pathway in a variety of cell lines (19,36,37). Importantly, Rab5 and Rab7 have been used to label early/sorting endosomes and late endosome/lysosomes, respectively (38,39). To characterize the EEA1-positive endocytic structures, Rab5A (Figure 1G) or Rab7A (Figure 1H) fused with fluorescent proteins (FPs) were transiently overexpressed and quantitatively co-localized with EEA1 immunostaining in MCF10A, T47D and MDAMB231 cells (Figure 1I). As expected, Rab5A-mRFP strongly colocalized with EEA1 (Pearson's >0.4), whereas Rab7A-dsRed displayed reduced colocalization with EEA1 staining (Pearson's ~0.1) in all three cell lines (Figure 1I, Table S5). Here, we showed that MCF10A cells overexpressing Rab5A-mRFP display irregular and large EEA1-positive aggregates at the perinuclear region (Figure 1G). In agreement, cells overexpressing wild-type Rab5 were shown previously to display larger endosomes containing both early and late endosome markers (40–42). In contrast, enlarged EEA1-positive endosomes were detected in both untransfected as well as in MDAMB231 and T47D cells overexpressing Rab5A-mRFP (Figure 1G, Figure S4). Moreover, overexpression of Rab7A-dsRed did not alter the endogenous EEA1 pattern and it is not found associated with the enlarged EEA1-positive endocytic structures in breast cancer cells (Figure 1H). In summary, EEA1-positive endosomes in human breast cancer cells also displayed AP3, Rab5 and internalized labeled-Tf, but lacked Rab7 and autophagy marker LC3, confirming their non-autophagic EE nature.

To characterize the early and recycling endosomes in breast cancer cells at the nanometer range, 3D *d*STORM SR microscopy was performed at 30–50 nm in the XY and 50 nm in the Z-axis (43,44). Cells were incubated with AF647-Tf for 1 h to label both the early and recycling compartments followed by immunostaining with anti-EEA1. Several representative regions of interest (ROI) are shown at high magnification in Figure 2A

(original field-of-view is shown in Figure S5) and 3D rotations of each ROI are shown in Video S1.MCF10A cells showed smaller EEA1- (red) and Tf-positive (green) vesicles with an average diameter of ~323 nm (Figure 2A, **panels a-e, q**) as well as numerous Tf-positive tubular structures (Figure 2A, **panels a-c, arrows**) that on average display ~750 nm in length and 150 nm in width (Figure 2A, **panels p**). MDAMB231 and T47D breast cancer cells displayed large EEA1- and Tf-positive vesicles with an average diameter of ~1500 nm and ~900 nm, respectively (Figure 2A, **panels f-j, k-o, q**; Table S6). The high spherical index of a large MDAMB231 vesicle is shown in Video S2. These results indicate that the enlarged endosomes, observed in breast cancer cells, comprised spherical vesicles of varying sizes without detectable tubular structures, as detected in MCF10A, although their existence cannot be completely excluded. Overall, these 3D dSTORM qualitative results suggest that breast cancer and non-cancerous cells exhibit a different nanoscale organization of EE compartments.

A quantitative 3D whole-cell imaging analysis of endogenous EE structures was developed using Imaris software (Bitplane, Inc) to generate and analyze the 3D rendering of these endosomal objects on a cell-by-cell basis (Figure S6). This analysis was applied to MDAMB231 and T47D breast cancer cells and non-cancerous MCF10A immunostained with anti-EEA1 (red) and anti-TfR (green) (Figure 2B). The EE morphology was analyzed without prolonged serum starvation to avoid induction of autophagy (33). MCF10A cells displayed an average of 469 3D-rendered EEA1 objects per cell (Figure 2C), which was significantly more than MDAMB231 and T47D cells (Table S7). In comparison, an early electron microscopy study of baby hamster kidney cells reported 300–400 EEs per cell (45). In contrast, the average volume of 3D-rendered EEA1-positive objects (Figures 2D), and the average length of the longest side (Figure S7A), were higher per cell in MDAMB231 vs. MCF10A and T47D cells. However, MCF10A cells had significantly higher total volume of 3D-rendered EEA1 objects as a % of cell volume (Figure 2E; Figure S7B) when compared to either breast cancer cell line. EEs are typically located closer to the cell surface to maintain normal function (46). To determine the distance of EEA1 to the plasma membrane, the 3D Euclidian distance was calculated, and then averaged per cell. Interestingly, the EEA1-positive endosomes in MDAMB231 cells were located further away from the plasma membrane when compared to either MCF10A or T47D cells (Figure 2F). In summary, MDAMB231 cells had on average fewer, but larger in volume and length, EEA1-positive endosomes, that were located further from the cell surface when compared to MCF10A cells. Interestingly, non-cancerous MCF10A showed a significantly larger total EE volume as a % of cell volume than human breast cancer cell lines, MDAMB231 and T47D. These quantitative results demonstrate significant adaptations in the EE morphology in breast cancer cells vs. non-cancerous cells.

Disrupted cargo sorting, endosome maturation and recycling in human breast cancer cells

Maturation of EEs with EGF-EGFR complexes into late endosomes leads to the termination of EGFR-mediated signaling and eventual receptor degradation. We hypothesized that if endosomal maturation is occurring normally in breast cancer cells, then colocalization between EEA1 and EGF should decrease over time as EGF-EGFR complexes are sorted out from EEA1-positive endosomes into maturing late endosomes for delivery to lysosomes.

Since AF488-EGF uptake by T47D cells was nearly undetectable, only MCF10A and MDAMB231 were included in this analysis. Quantitative analysis showed that colocalization of EGF with EEA1, as shown by Pearson's coefficient of whole-cell z-stacks, decreased significantly from 10 min to 60 min in MCF10A cells (Figure 3A–B), but not in MDAMB231 cells (Figure 3A–B; Table S8). Internalized EGF remains colocalized with EEA1 for longer periods of time in MDAMB231 than in MCF10A cells, suggesting that EGF delivery to late endosomes is delayed in MDAMB231 cells.

Endocytic recycling of Tf-TfR from EEs to the cell surface is required for iron homeostasis and cell proliferation (10). Significantly more Tf remained intracellularly in T47D compared to MCF10A using a Tf-TfR recycling assay, suggesting that T47D cells displayed a dramatically slower overall recycling pathway (Figure 3C, Table S9). In contrast, MDAMB231 cells retained significantly more Tf than MCF10A only at the early chase time points (5–30 min) (Figure 3C, Table S9), suggesting that MDAMB231 cells showed reduced fast recycling pathway compared to MCF10A cells.

Live-cell pulse-chase imaging of fluorescently-labeled Tf, LDL and EGF was performed in MCF10A vs. MDAMB231 cells (Figure 3D and Video S3) to follow the intracellular trafficking of labeled ligands during the early time points of endocytic pathway (4–14 min), which include the Tf fast recycling pathway as well as the EGF early to late endosome maturation step. Importantly, the endogenous protein levels of TfR and LDLR were similar between MCF10A and MDAMB231 cells, while EGFR expression was slightly higher in MDAMB231 than MCF10A (Figure S8A–D, Table S10). At 4 min, MCF10A cells showed a perinuclear Tf pattern with peripherally distributed EGF and LDL punctate structures. In contrast, MDAMB231 cells displayed endosomes containing all three ligands that were distributed throughout the cell. To determine the ligand composition of endocytic populations over time, a morphometric quantification based on 3D-rendered endocytic objects containing each ligand was performed (Figure S9A–D, Table S11). In Figure 3D–E, MCF10A cells showed a decreasing population of EGF objects containing Tf or Tf + LDL ligands over time in comparison to MDAMB231 cells, reflecting a faster Tf recycling back to the plasma membrane in MCF10A cells. In Figure S9C, the average number of intracellular Tf containing vesicles also showed a faster decrease in MCF10A than in MDAMB231 cells. Moreover, in Figure S9D, the % of vesicles carrying only Tf and thus directly involved in the fast recycling pathway decrease over time more rapidly in MCF10A than in MDAMB231 cells. In agreement with Figure 3C, these results suggest that, in comparison to MCF10A cells, MDAMB231 cells have a decreased fast recycling pathway.

Time-lapse ligand trafficking experiments shown in Figure 3D–E can also be used to follow the EGF early to late endosome maturation trafficking step. Kinetically, LDL is a known marker of the late endosomal/lysosomal pathway since its release from LDLR occurs upon endosomal acidification as the early endosomes mature into late endosomes(8,47). Thus, during early time-points of endocytic trafficking, cargo delivery to the late endosomal/lysosomal pathway can be followed using labeled-LDL. Initially, at 4 min, 49% of the EGF objects contained LDL in MCF10A, while only 7% of LDL-containing EGF vesicles were detected in MDAMB231 cells (Figure 3E, Figure S9A). Conversely, the percent of endosomes containing both labeled EGF and Tf was very low (< 2.3%) in MCF10A

compared to that in MDAMB231 cells (~27%) (Figure 3E, Figure S9A, Table S11). At 14 min, in MCF10A, 52% of EGF were localized with LDL, indicating their delivery to the late endosomal/lysosomal pathway (1,8). In contrast, in MDAMB231 cells, EGF-positive vesicles showed reduced accumulation of LDL ligands and furthermore 50% of EGF-positive vesicles contained EGF only at 14 min, suggesting a delayed delivery to late endosomes. In Figure S9A, %EGF- and -LDL-positive vesicles remain at 45–60% in MCF10A, whereas they increase over time from 5–30% in MDAMB231 cells. Overall these results suggest a delay in endosomal maturation in MDAMB231 cells, leading to the retention of EGF in EE containing either EGF only or EGF plus Tf. In summary, our results suggest that the dynamic endosomal sorting of EGF, LDL and Tf ligands differs significantly between MCF10A and MDAMB231 cells.

Increased EGF-dependent activation of EGFR-p1068 in MDAMB231 EEs

EGF-induced activation of EGFR results in protein dimerization and autophosphorylation at multiple locations within the cytoplasmic domain, including tyrosine 1068 (48,49). We hypothesized that EGF-induced activation of EGFR is upregulated and/or prolonged in MDAMB231 cells, since our data showed extended colocalization of EGF with EEA1 and delayed EGF endocytic sorting and maturation in MDAMB231 cells. AKT and ERK1/2 are well-known to be activated indirectly following EGF-mediated EGFR activation (50). Here, EGF-induced activation of EGFR-p1068 (Figure 4A–C), phosphorylated AKT (pAKT) and ERK1/2 (pERK1/2) (Figure S10A–D) were evaluated in whole cell lysates via immunoblotting assays. Firstly, EGFR-p1068, pAKT and pERK1/2 levels were determined in MCF10A and MDAMB231 cells subjected or not to 5 min EGF stimulation on a single immunoblot membrane (Figure 4A, Figure S10A). Unstimulated MDAMB231 cells showed a higher baseline of pAKT and pERK1/2 signaling, due to the KRAS mutation present in MDAMB231 cells (7). Importantly, the signaling results agreed whether cell lysates were analyzed in single (Figure 4A, Figure S10A) or separate (Figure 4B–C, Figure S10B–D) membranes. Upon EGF stimulation, the MCF10A and MDAMB231 cells showed significant increases in EGFR-p1068 (Figure 4B–C) and pAKT levels, that peaked at 5 min in both cell lines (Figure S10C). The pERK1/2 response peaked at 5–10 min, with each cell line returning to pre-stimulation levels within 15 min (Figure S10D). Interestingly, the extent of EGFR-p1068 and pAKT signaling was significantly increased in MDAMB231, compared to MCF10A cells (Figure S10C, Table S12). In addition, while MCF10A returned to pre-stimulation levels for EGFR-p1068 by 10 min, the activity of EGFR-p1068 in MDAMB231 remained elevated after 30–60 min (Figure 4B, Table S12). These results generated in whole cell lysates, indicate an increased and extended EGFR-p1068 activation in MDAMB231 cells, which is in concordance with a reduction in EGFR deactivation due to delayed endocytic maturation.

Additionally, a detailed analysis of EGFR-p1068 activation at the sub-cellular level was performed to assay the role of endocytic morphology in EGFR signaling (Figure 4D–E, Figure S11). Prior to EGF stimulation, a few EGFR-containing endosomes were detected in MDAMB231 (Figure 4D, **0 min**). Upon EGF stimulation, major changes in the size, intensity and distribution of EGFR and EGFR-p1068 containing endosomes were detected in both MCF10A and MDAMB231 cells (Figure 4D, **5–60 min**; Figure S12A). Consistent with

the immunoblotting assays, EGFR-p1068 activation in MCF10A cells increased from 0–10 min before a rapid decline to steady-state levels at 60 min (Figure 4E, i, Table S13A). In MDAMB231 cells, EGFR activation peaked at 15 min before a slow decline of p1068 intensity levels that remained higher than prior to EGF stimulation, even at 60 min (Figure 4E, i, Table S13A). To determine if the extent or duration of EGFR-p1068 activation correlated with the endocytic volume, the total 3D rendered EGFR object population was split at their median volume ($\sim$0.04 μm^3), leading to a similar number of endocytic objects in each population evaluated (Figure S11 and S12B). In Figure 4D, the 3D-rendered endosomes were pseudo-colored based on the intensity levels of EGFR-p1068. The increase in EGFR-p1068 activation was detected predominantly in the larger 3D EGFR population (>0.04 μm^3) of MDAMB231 (Figure 4E, iii). In agreement, the volume of EGFR endosomes was significantly larger in MDAMB231 than in MCF10A cells prior to EGF stimulation at 0 min; upon EGF stimulation, the endosomal volume increased even further at 10 min without significant change from 10 to 60 min (Figure 4E, iv, Table S13B). Moreover, EGFR and EGF mean intensity in 3D EGFR objects peaked at 15min in both cells (Figure 4E, v–vi). However, higher levels were maintained throughout the remaining of the EGF stimulation period in MDAMB231 cells (Figure 4E, v), suggesting that increased EGFR-p1068 activation is due to retention in EE compartments. In summary, these results show that MDAMB231 cells exhibit enhanced and prolonged activation of EGFR following EGF stimulation compared to MCF10A cells. Furthermore, a population of enlarged endosomes is responsible for the more dramatic changes in EGFR-p1068 activation levels. Prolonged EGFR activation correlates with extended presence of EFG-EGFR, possibly due to increased retention of the EGF-EGFR complexes within an enlarged endosomal population of MDAMB231 cells.

Rab4A modulates endosomal size

While Rab4 and Rab11 have coordinated functions, Rab4A is highly associated with the fast recycling pathway and EGFR regulation, while Rab11 is connected to the slow recycling pathway (18–20,22,23). Moreover, the downregulation of EGFR activation has been suggested to occur primarily before ESCRT-mediated late endosomal trafficking, although this process may be altered in some forms of cancer (12). However, the observed changes in trafficking behavior (Figure 3) or endocytic volume (Figure 2) between cell lines could not be directly correlated to changes in endogenous expression of Rab5, Rab4, Rab11 or Rab7 (Figure S8E, Table S10). To address the spatial relationship of Rab4A or Rab11A with respect to EEA1-positive EEs, Rab4A or Rab11A fluorescent protein fusion constructs were expressed in MCF10A, MDAMB231 and T47D cells and subjected to colocalization analysis with endogenous EEA1 staining (Figure 5A–C). As expected, Rab4A-mCherry strongly colocalized with EEA1 (Pearson's >0.4), whereas Rab11A-EGFP showed a slightly decreased colocalization (Pearson's $\sim$0.2–0.4) (Figure 5C, Table S5). Interestingly, MCF10A cells overexpressing Rab4A display several enlarged EEA1-positive endosomes, when compared to untransfected cells (Figure 5A), a pattern that was reminiscent of that found in untransfected MDAMB231 cells. Overexpressing of Rab11A-EGFP did not alter the endogenous EEA1 pattern (Figure 5B).

Since endogenous EEA1 pattern in MCF10A, but not in MDAMB231 cells, is altered upon overexpression of wild-type (WT) Rab4A (Figure 5A), we hypothesized that the size of 3D-rendered EEA1 endosomes could be modulated by the overexpression of the constitutively-active Rab4A [Rab4A-CA; Q67L mutation; (51)] or the dominant-negative Rab4A [Rab4A-DN; N121I mutation; (51)]. Thus, Rab4A-WT, -CA and -DN EGFP constructs were transiently overexpressed in MCF10A (Figure 5D) and MDAMB231 (Figure 5E), followed by immunostaining with anti-EEA1. The 3D-rendered EEA1 average object size is significantly increased in MCF10A cells overexpressing Rab4A-WT-EGFP compared to untransfected cells (Figure 5F, Table S14). In MDAMB231 cells, a slight but significant increase in the average size of the 3D-rendered EEA1 objects was determined in Rab4A-WT-EGFP overexpressed cells when compared to untransfected cells (Figure 5H, Table S14). Surprisingly, the overexpression of Rab4A-CA or Rab4A-DN in MCF10A or MDAMB231 cells did not alter the size of 3D EEA1 objects compared to untransfected MCF10A (Figure 5F, 5H, Table S14). Importantly, in both MCF10A and MDAMB231, colocalization of EEA1 and Rab4A-WT was significantly higher than that between EEA1 and either Rab4A-CA or Rab4A-DN (Figure 5G, 5I, Table S15). This may explain the lack of effect of these mutants on endosomal size. In summary, the overexpression of Rab4A-WT increases EEA1 endosomal size in both MCF10A and MDAMB231 cells. In contrast, Rab4A mutations that lead to constitutive Rab4A activation or inhibition, but lack endosomal localization, do not alter EEA1 endosomal size.

To determine the role of Rab4A depletion on endosomal size, a lentiviral Rab4A-shRNA was used in both MCF10A (Figure 5J) and MDAMB231 (Figure 5K). Cells with a 50% or more Rab4A depletion were utilized, as determined by immunoblotting assay (**MCF10A**: Figure 5L**; MDAMB231**: Figure 5N), Negative control cells were infected with empty vector (EV-control). The endosomal size of EEA1 3D objects and the whole cell signaling response to EGF stimulation were evaluated. Upon visual inspection, the MCF10A EV-control cells display the typical EEA1 pattern associated with endogenous MCF10A (Figure 5J, **left**). Surprisingly, the MCF10A shRab4A-KD cells displayed enlarged EEA1 endosomes that were significantly larger than those detected in MCF10A EV-control cells (Figure 5J, **right and** 5M, Table S16), suggesting that Rab4A levels must be tightly controlled to maintain endosomal size. Rab4A knockdown in MDAMB231 cells, in contrast, did not lead to significant changes in endosomal size (Figure 5K, 5O). This could be attributed to a much higher relative expression of Rab4B mRNA in MBAMD231 cells, compared to MCF10A cells (Figure S13). Figure 5N validates this antibody against Rab4 as specific towards Rab4A. Therefore, Rab4A protein expression is also decreased in MDAMB231, in comparison with MCF10A (Figure S8A). These results suggest a complex and cell-specific Rab4-mediated regulation of endosomal size.

Complex Rab4A modulation of EGFR activation in enlarged EEs

To determine if Rab4A overexpression or depletion affects EGF-induced EGFR-p1068 activation and the phosphorylation of AKT and ERK1/2 at a global level, whole cell immunoblots were analyzed as shown in Figure 6A and Figure S14 and S15. MCF10A cells were infected with either Rab4A-myc or empty vector (EV). Following EGF stimulation, no difference was found between Rab4A-myc and EV for EGFR-p1068, AKT and ERK1/2

phosphorylation levels in whole cell lysates (Figure 6A–i; Figure S15, Table S17). The EGF-mediated EGFR-p1068 or pAKT activation levels were also similar in both shRab4A-KD and EV-control MCF10A cells (Figure 6A–ii, Figure S14A–B & D). There was a significant increase in pERK1/2 following EGF stimulation in the shRab4A-KD compared to EV-control in MCF10A cells (Figure S14C–D, Table S18). Moreover, the shRab4A-KD MDAMB231 cells displayed a significant increase in EGFR-p1068, but not pAKT, upon EGF stimulation compared to EV-control (Figure 6A–iii, Figure S14E–F).

To further test the role of Rab4A on the EGF-induced activation of EGFR-p1068 in enlarged endosomes, Rab4A-EGFP or EV-EGFP were overexpressed in MCF10A cells. Then, these cells were subjected to the activated EGFR-p1068 image analysis methodology (Figure 6B–C), as described in Figure 4D–E and Figure S11. To allow for the visual representation of the activated EGFR-p1068 according to endosome size, the 3D-rendered EGFR endosomal objects were split at above and below $0.04 \ \mu m^3$ and pseudo-colored according to EGFR-p1068 mean intensity (Figure 6B–C, Figure S16). This resulted in a population consisting of 40–60% of total number of endosomal objects, at any given time (Figure S16B). Upon addition of EGF, an increased number of EGFR-containing vesicles, as well as an elevated level of activated EGFR-p1068 was detected (Figure 6B–C). Quantitative analysis indicates an increased activation of EGFR-p1068 in Rab4A-EGFP following EGF simulation from 10–60 min, compared to MCF10A overexpressing EV-GFP (Figure 6C, i–iii Figure S16A, Table S19). Larger endosomes ($>0.04 \ \mu m^3$) displayed significantly higher EGFR-p1068 activation levels in Rab4A-EGFP overexpressed cells (Figure 6C, iii). Strikingly, the intensity of EGFR-p1068 in the Rab4A-EGFP remained above steady state levels in the larger endosomal populations (Figure 6C, ii–iii). In agreement, EGF stimulation induced an increased endosomal size in the larger population of 3D EGFR objects in Rab4A-EGFP overexpressed MCF10A cells (Figure 6C, iv–vi). These results show that Rab4A overexpressing MCF10A cells exhibit enhanced and prolonged EGF-mediated EGFR-p1068 activation compared to EV-transfected MCF10A cells. Moreover, a population of enlarged endosomes is responsible for the more dramatic changes in EGFR-p1068 activation in the Rab4A overexpressing MCF10A cells. This result, however, contrasts with the whole-cell lysate EGFR immunoblotting analysis showing no change in total EGFR activation levels upon Rab4A overexpression (Figure 6A). Since the effect of Rab4A overexpression on EGFR-p1068 activation and EGFR 3D object volume (Figure 6B–C) was predominantly detected on the larger endosomal population ($>0.04 \ \mu m^3$), this effect could be diluted in the whole cell analysis. In summary, the prolonged EGFR-p1068 activation upon Rab4A overexpression in MCF10A cells occurs mainly in an enlarged endosomal population. This data underlies the cell line specificity and the complexity of Rab4's role in the regulation of endosomal size and EGFR signaling.

DISCUSSION

EEs have been shown to be altered in various forms of cancer (6,52). Moreover, clinical and translational data have described significant correlations between increased Rab4, Rab5 and Rab11 expression levels and human cancer progression and aggressiveness (4,53). The recently proposed "adaptive endocytosis" hypothesis entails that cancer cells can modify their endocytic trafficking pathways to alter signaling and enhance their proliferative and

survival properties (3). However, a comparison of endosomal morphology and function across human cancer cell lines has been lacking. Our results reveal dramatic heterogeneity in EE morphology in a panel of non-cancerous MCF10A and four breast cancer cell lines. MDAMB231 display large perinuclear endosomes containing EE markers such as EEA1, AP3, Rab4 and Rab5. In contrast, MCF10A have smaller, more numerous and evenly distributed endosomes that contain similar EE markers. Moreover, these EEA1-positive endosomes lack both Rab7 and autophagy marker LC3, confirming their EE nature in both cell lines. Importantly, enlarged EEA1-positive EEs were also observed in tumor tissue sections from two distinct human tumor xenograft models. 3D STORM microscopy characterized the enlarged EE in MDAMB231 and T47D as highly spherical vesicles, sometimes larger than 1000nm in diameter and lacking the distinct Tf-positive recycling tubules that were observed in MCF10A. This data indicates that at least some breast cancer cells may be deficient in the tubular endocytic structures associated with Rab4, Rab11 and retromer regulation (9,19). Fluorescently-labeled ligand uptake live-cell imaging results together with the endosomal morphometric data, suggest that breast cancer cells show an alternative organization of their early endosomal pathway, in which different cargo, such as Tf and EGF accumulate along the endosomal pathway in larger but fewer perinuclear endosomes. These results show that breast cancer cells display a functional, although altered, EE compartment involved in Tf recycling and EGF-mediated signaling. These adaptations of the early endosomal pathway could be advantageous to breast cancer cells by facilitating efficient cargo delivery and modulating receptor signaling for their increased metabolic and cell proliferation requirements (3).

One hypothesis is that modulation of endosome size can be achieved by altering endosomal fusion and fission machinery (54,55). For example, overexpression of Rab5A-CA (36) results in irregular, large and perinuclear endosomal aggregates containing EEA1, Rab5 and Rab7 (56). Rab5 effectors can also influence endosomal size via overexpression of Rabanykrin-5, which was shown to produce enlarged, peripheral Rab5 endosomes, while specifically excluding EEA1 (57). Here, we found that Rab4A-WT overexpression leads to enlarged EEA1-positive endosomes in both MCF10A cells and MDAMB231 cells. Previously, Rab4 overexpression appeared to not alter endosome morphology in A431 and HeLa cells (19,37). This apparent contradiction in Rab4's effect on endosomal morphology may be related to its pleomorphic nature (45) and diverse morphology across cell types (8), stressing the necessity to use high-resolution imaging to visualize and quantitate endosomal size and morphology in various breast cancer cells. Interestingly, we have shown that overexpression of Rab4A-CA or Rab4A-DN does not alter endosomal size, which is likely connected to the lack of localization of these mutant Rab4A forms to EEA1-positive EE compartments in both MCF10A and MDAMB231 cells. Recently, a Rab4, Rabaptin and Rabex feed-forward loop has been described as a requirement for the continued activation of Rab5 at the EE (58). The role of Rab4 activity in the feed-forward activation of Rab5 would support the importance of Rab4 cycling in the stabilization of large EEs. Thus, these results suggest that for Rab4A to modulate EEA1 endosomal size it must not only localize to the EE but also be capable of cycling between a GDP-GTP state.

Herein, we have demonstrated that Rab4A is a modulator of endocytic volume since Rab4A overexpression leads to increased endosomal size in both MCF10A and MDAMB231,

whereas knockdown of Rab4A results in increased endosomal size in MCF10A but not in MDAMB231 cells. Previously, similar results have been shown in other cell types (59–61), suggesting that precise control of Rab4 expression regulates EE volume in a cell-specific manner. Considering that Rab4 has been shown to be involved in both membrane fusion and fission events (58,62), changes in Rab4 expression could result in increased EE size. We propose a basic model (Figure S17), where Rab4A overexpression leads to increased vesicle fusion, likely in a Rab5 and EEA1 dependent manner, resulting from the stabilization of Rab5 activity by Rab4 (58). Rab4 overexpression is not expected to increase fission and budding events, since Rab4's involvement in vesicle formation requires its interaction with several effector proteins, such as D-AKAP2, an effector that regulates Rab4/Rab11-dependent endocytic recycling (18,63) and Arl1, a GTPase that controls endosomal budding sites, adapter protein recruitment and endosomal size (51). Therefore, Rab4A depletion may result in increased EE size via a reduction of fission and budding (recycling) events. Although, Rab4A has been the most extensively studied member of the Rab4 family, Rab4B has been suggested to also be involved in the regulation of the early and recycling endocytic pathways (64). Based on EMBOSS Stretcher global pairwise analysis Rab4A and Rab4B share 84.7% identity and 89.6% similarity, which would strongly suggest a common functionality (65). Interestingly, RT-qPCR has detected significantly elevated Rab4B RNA levels in MDAMB231 cells, in comparison to MCF10A cells (Figure S13). Therefore, an alternative hypothesis to explain the overexpression/depletion Rab4A results may include Rab4B-mediated compensatory effects.

We have investigated EGFR-mediated signaling in MCF10A and MDAMB231 cells, which do not possess specific EGFR mutations. However, MDAMB231 cells show elevated levels of KRAS expression and carry a KRAS mutation (KRAS G13D) that could affect endosomal trafficking via PI-3 kinase and RAS signaling pathways (29,66,67). Both whole-cell lysate and imaging signaling assays showed an increased and extended EGF-mediated EGFR-p1068 activation in MDAMB231, which is most probably due to delayed endosomal sorting and maturation. In addition, the subcellular imaging method used in this paper to assay EGFR-p1068 signaling appears ideally suited for situations where the majority of signaling endosomes are behaving similarly within a given cell. Overall, our data suggests that upon EGF stimulation, EGF-EGFR complexes are rapidly transported to enlarged pre-existing EE vesicles in MDAMB231 cells, where EGF-mediated signaling remains activated for prolonged periods, when compared to MCF10A. Importantly, this data is consistent with previous results suggesting that endosomal size can affect EGFR signaling, cell differentiation and cancer progression (54,68–72). Our results indicate that after stimulation with EGF, enlarged endosomal size correlates with prolonged EGFR activation and delayed endocytic maturation. However, Rab4A knockdown MDAMB231 cells display an unaltered enlarged endosomal morphology as well as elevated EGF-mediated pEGFR-p1068 activation levels, in contrast to Rab4A depleted MCF10A cells, which show increased endosomal size as well as pERK1/2 activation levels. These results suggest a distinct regulatory mechanism for the endosomal size and EGFR signaling in MCF10A vs. MDAMB231 cells. Rab4A appears to be a crucial driver of the relationship between prolonged EGF-induced signaling and enlarged endosomal size in MCF10A cells. In contrast, altered Rab4A/Rab4B ratios may be at the basis of a complex regulatory

mechanism of endosomal size and receptor-mediated signaling in MDAMB231 cells. Even in the absence of overall changes in whole cell-based signaling activation levels, localized changes in receptor tyrosine kinase signaling may be critical for multiple processes such as polarity, migration and invasion, raising the possibility that crosstalk between endosomal regulators, the cytoskeleton and the plasma membrane may drive breast cancer tumorigenesis (1,73,74).

In conclusion, we show that significant EE heterogeneity can occur in non-cancerous and breast cancer cells, both in terms of size, location and receptor cargo composition. Furthermore, these results propose Rab4 as a regulator of the biogenesis of large EE vesicles that allow for prolonged activation of signaling receptors both in non-cancerous as well as breast cancer cells. Therefore, we suggest that alterations in EE morphology, size, trafficking and distribution can affect receptor-mediated signaling in breast cancer cells.

Supplementary Material

Refer to Web version on PubMed Central for supplementary material.

Acknowledgements

Abbreviations

3D dSTORM	3D direct stochastic optical reconstruction microscopy
AF	Alexa Fluor
AP3	Adaptor protein 3
APPL1	adaptor protein containing PH domain, PTB domain and leucine zipper motif 1
BSA	bovine serum albumin
CA	constitutively active
CI	clear imaging
DN	dominant negative
EE	early endosome
EEA1	early-endosome antigen-1

EGFP	enhanced green fluorescent protein
EGF	epidermal growth factor
EGFR	epidermal growth factor receptor
EGFR-p1068	epidermal growth factor receptor phosphorylation at tyrosine 1068
ESCRT	endosomal sorting complexes required for transport
FBS	fetal bovine serum
FPs	Fluorescent proteins
HMEC	human mammary epithelial cell
LC3	Microtubule-associated proteins 1A/1B light chain 3B
LDL	low-density lipoprotein
LDLR	low-density lipoprotein receptor
MIP	maximum intensity projection
ROI	region of interest
SR	super-resolution
Tf	transferrin
TfR	transferrin receptor
WT	wild-type

REFERENCES

1. Mellman I, Yarden Y. Endocytosis and cancer. Cold Spring Harb Perspect Biol. 2013;5:a016949. [PubMed: 24296170]

2. Parachoniak CA, Park M. Dynamics of receptor trafficking in tumorigenicity. Trends Cell Biol. 2012;22:231–40. [PubMed: 22397948]

3. Schmid SL. Reciprocal regulation of signaling and endocytosis: Implications for the evolving cancer cell. J Cell Biol. 2017;216:2623–32. [PubMed: 28674108]

4. Frittoli E, Palamidessi A, Marighetti P, Confalonieri S, Bianchi F, Malinverno C, et al. A RAB5/ RAB4 recycling circuitry induces a proteolytic invasive program and promotes tumor dissemination. J Cell Biol. 2014;206:307–28. [PubMed: 25049275]

5. Elkin SR, Bendris N, Reis CR, Zhou Y, Xie Y, Huffman KE, et al. A systematic analysis reveals heterogeneous changes in the endocytic activities of cancer cells. Cancer Res. 2015;75:4640–50. [PubMed: 26359453]

6. Johnson IRD, Parkinson-Lawrence EJ, Shandala T, Weigert R, Butler LM, Brooks DA. Altered Endosome Biogenesis in Prostate Cancer Has Biomarker Potential. Mol Cancer Res. 2014;12:1851– 62. [PubMed: 25080433]

7. Basu SSK, Lee S, Salotti J, Basu SSK, Sakchaisri K, Xiao Z, et al. Oncogenic RAS-Induced perinuclear signaling complexes requiring KSR1 regulate signal transmission to downstream targets. Cancer Res. 2018;78:891–908. [PubMed: 29259016]

8. Maxfield FR, McGraw TE. Endocytic recycling. Nat Rev Mol Cell Biol. 2004;5:121–32. [PubMed: 15040445]

9. Naslavsky N, Caplan S. The enigmatic endosome – sorting the ins and outs of endocytic trafficking. J Cell Sci. 2018;131:jcs216499. [PubMed: 29980602]

10. Luck AN, Mason AB. Transferrin-Mediated Cellular Iron Delivery. Curr Top Membr. 2012;69:3–35. [PubMed: 23046645]

11. Rink J, Ghigo E, Kalaidzidis Y, Zerial M. Rab conversion as a mechanism of progression from early to late endosomes. Cell. 2005;122:735–49. [PubMed: 16143105]

12. Tomas A, Futter CE, Eden ER. EGF receptor trafficking: Consequences for signaling and cancer. Trends Cell Biol. 2014;24:26–34. [PubMed: 24295852]

13. Pfeffer SR. Rab GTPase regulation of membrane identity. Curr Opin Cell Biol. 2013;25:414–9. [PubMed: 23639309]

14. Kalaidzidis I, Miaczynska M, Brewinska-Olchowik M, Hupalowska A, Ferguson C, Parton RG, et al. APPL endosomes are not obligatory endocytic intermediates but act as stable cargo-sorting compartments. J Cell Biol. 2015;211:123–44. [PubMed: 26459602]

15. Flores-Rodriguez N, Kenwright DA, Chung P-H, Harrison AW, Stefani F, Waigh TA, et al. ESCRT-0 marks an APPL1-independent transit route for EGFR between the cell surface and the EEA1-positive early endosome. J Cell Sci. 2015;128:755–67. [PubMed: 25588841]

16. Agola JO, Jim PA, Ward HH, Basuray S, Wandinger-Ness A. Rab GTPases as regulators of endocytosis, targets of disease and therapeutic opportunities. Clin Genet. 2011;80:305–18. [PubMed: 21651512]

17. Di Fiore PP, von Zastrow M. Endocytosis, signaling, and beyond. Cold Spring Harb Perspect Biol. 2014;6:a016865. [PubMed: 25085911]

18. Eggers CT, Schafer JC, Goldenring JR, Taylor ST. D-AKAP2 interacts with Rab4 and Rab11 throughi its RGS domains and regulates transferrin receptor recycling. J Biol Chem. 2009;284:32869–80. [PubMed: 19797056]

19. Sönnichsen B, De Renzis S, Nielsen E, Rietdorf J, Zerial M. Distinct membrane domains on endosomes in the recycling pathway visualized by multicolor imaging of Rab4, Rab5, and Rab11. J Cell Biol. 2000;149:901–13. [PubMed: 10811830]

20. Mohrmann K, Gerez L, Oorschot V, Klumperman J, van der Sluijs P. Rab4 function in membrane recycling from early endosomes depends on a membrane to cytoplasm cycle. J Biol Chem. 2002;277:32029–35. [PubMed: 12036958]

21. van der Sluijs P, Hull M, Webster P, Mâle P, Goud B, Mellman I. The small GTP-binding protein rab4 controls an early sorting event on the endocytic pathway. Cell. 1992;70:729–40. [PubMed: 1516131]

22. Goueli BS, Powell MB, Finger EC, Pfeffer SR. TBC1D16 is a Rab4A GTPase activating protein that regulates receptor recycling and EGF receptor signaling. Proc Natl Acad Sci U S A. 2012;109:15787–92. [PubMed: 23019362]

23. McCaffrey MW, Bielli A, Cantalupo G, Mora S, Roberti V, Santillo M, et al. Rab4 affects both recycling and degradative endosomal trafficking. FEBS Lett. 2001;24791:1–10.

24. Ceresa BP. Regulation of EGFR endocytic trafficking by rab proteins. Histol Histopathol. 2006;21:987–93. [PubMed: 16763949]

25. Marsh M, Griffiths G, Dean GE, Mellman I, Helenius A. Three-dimensional structure of endosomes in BHK-21 cells. Proc Natl Acad Sci U S A. 1986;83:2899–903. [PubMed: 3458249]

26. Abe K, Zhao L, Periasamy A, Intes X, Barroso M. Non-invasive in vivo imaging of near infrared-labeled transferrin in breast cancer cells and tumors using fluorescence lifetime FRET. PLoS One. 2013;8:e80269. [PubMed: 24278268]

27. Rudkouskaya A, Sinsuebphon N, Ward J, Tubbesing K, Intes X, Barroso M. Quantitative Imaging of Receptor-Ligand Engagement in Intact Live Animals. J Control Release. 2018;286:451–9. [PubMed: 30036545]

28. Das A, Nag S, Mason AB, Barroso MM. Endosome-mitochondria interactions are modulated by iron release from transferrin. J Cell Biol. 2016;214:831–845. [PubMed: 27646275]

29. Smith SE, Mellor P, Ward AK, Kendall S, McDonald M, Vizeacoumar FSFJV, et al. Molecular characterization of breast cancer cell lines through multiple omic approaches. Breast Cancer Res. Breast Cancer Research; 2017;19:1–12. [PubMed: 28052757]

30. Neve RM, Chin K, Fridlyand J, Yeh J, Baehner FL, Fevr T, et al. A collection of breast cancer cell lines for the study of functionally distinct cancer subtypes. Cancer Cell. 2006;10:515–27. [PubMed: 17157791]

31. Holliday DL, Speirs V. Choosing the right cell line for breast cancer research. Breast cancer Res. 2011;13:215. [PubMed: 21884641]

32. Aaron JS, Taylor AB, Chew TL. Image co-localization - co-occurrence versus correlation. J Cell Sci. 2018;131:jcs211847. [PubMed: 29439158]

33. Mizushima N, Yoshimori T, Levine B. Methods in Mammalian Autophagy Research. Cell. 2010;140:313–26. [PubMed: 20144757]

34. Saftig P, Klumperman J. Lysosome biogenesis and lysosomal membrane proteins: Trafficking meets function. Nat Rev Mol Cell Biol. 2009;10:623–35. [PubMed: 19672277]

35. Park SY, Guo X. Adaptor protein complexes and intracellular transport. Biosci Rep. 2014;34:381–90.

36. Ceresa BP, Lotscher M, Schmid SL. Receptor and Membrane Recycling Can Occur with Unaltered Efficiency Despite Dramatic Rab5(Q79L)-induced Changes in Endosome Geometry. J Biol Chem. 2001;276:9649–54. [PubMed: 11136733]

37. Shin HW, Hayashi M, Christoforidis S, Lacas-Gervais S, Hoepfner S, Wenk MR, et al. An enzymatic cascade of Rab5 effectors regulates phosphoinositide turnover in the endocytic pathway. J Cell Biol. 2005;170:607–18. [PubMed: 16103228]

38. Feng Y, Press B, Wandinger-Ness A. Rab 7: An important regulator of late endocytic membrane traffic. J Cell Biol. 1995;131:1435–52. [PubMed: 8522602]

39. Chavrier P, Parton RG, Hauri HP, Simons K, Zerial M. Localization of low molecular weight GTP binding proteins to exocytic and endocytic compartments. Cell. 1990;62:317–29. [PubMed: 2115402]

40. Kaur G, Tan LX, Rathnasamy G, Cunza N La, Germer CJ, Toops KA, et al. Aberrant early endosome biogenesis mediates complement activation in the retinal pigment epithelium in models of macular degeneration. Proc Natl Acad Sci U S A. 2018;115:9014–9. [PubMed: 30126999]

41. Roberts RL, Barbieri MA, Pryse KM, Chua M, Morisaki JH, Stahl PD. Endosome fusion in living cells overexpressing GFP-rab5. J Cell Sci. 1999;112:3667–75. [PubMed: 10523503]

42. Hirota Y, Kuronita T, Fujita H, Tanaka Y. A role for Rab5 activity in the biogenesis of endosomal and lysosomal compartments. Biochem Biophys Res Commun. 2007;364:40–7. [PubMed: 17927960]

43. Rust MJ, Bates M, Zhuang X. Sub-diffraction-limit imaging by stochastic optical reconstruction microscopy (STORM). Nat Methods. 2006;3:793–5. [PubMed: 16896339]

44. Huang B, Wang W, Bates M, Zhuang X. Three-dimensional super-resolution imaging by stochastic optical reconstruction microscopy. Science. 2008;319:810–3. [PubMed: 18174397]

45. Griffiths G, Back R, Marsh M. A quantitative analysis of the endocytic pathway in baby hamster kidney cells. J Cell Biol. 1989;109:2703–20. [PubMed: 2592402]

46. Neefjes J, Jongsma MML, Berlin I. Stop or Go? Endosome Positioning in the Establishment of Compartment Architecture, Dynamics, and Function Trends Cell Biol. Elsevier Ltd; 2017;27:580–94. [PubMed: 28363667]

47. Zanoni P, Velagapudi S, Yalcinkaya M, Rohrer L, von Eckardstein A. Endocytosis of lipoproteins. Atherosclerosis. 2018;275:273–95. [PubMed: 29980055]

48. Francavilla C, Papetti M, Rigbolt KTG, Pedersen AK, Sigurdsson JO, Cazzamali G, et al. Multilayered proteomics reveals molecular switches dictating ligand-dependent EGFR trafficking. Nat Struct Mol Biol. 2016;23:608–18. [PubMed: 27136326]

49. Shostak K, Chariot A. EGFR and NF-κB: Partners in cancer. Trends Mol Med. 2015;21:385–93. [PubMed: 25979753]

50. Hsu JL, Hung MC. The role of HER2, EGFR, and other receptor tyrosine kinases in breast cancer. Cancer Metastasis Rev. 2016;35:575–88. [PubMed: 27913999]

51. D'Souza RS, Semus R, Billings EA, Meyer CB, Conger K, Casanova JE. Rab4 orchestrates a small GTPase cascade for recruitment of adaptor proteins to early endosomes. Curr Biol. 2014;24:1187–98. [PubMed: 24835460]

52. Silva P, Mendoza P, Rivas S, Díaz J, Moraga C, Quest AFG, et al. Hypoxia promotes Rab5 activation, leading to tumor cell migration, invasion and metastasis. Oncotarget. 2016;7:29548–62. [PubMed: 27121131]

53. Chalouni C, Doll S. Fate of Antibody-Drug Conjugates in Cancer Cells. J Exp Clin Cancer Res. 2018;37:1–12. [PubMed: 29301578]

54. Villaseñor R, Nonaka H, Del Conte-Zerial P, Kalaidzidis Y, Zerial M. Regulation of EGFR signal transduction by analogue-to-digital conversion in endosomes. Elife. 2015;4:1–32.

55. Foret L, Dawson JE, Villaseñor R, Collinet C, Deutsch A, Brusch L, et al. A general theoretical framework to infer endosomal network dynamics from quantitative image analysis. Curr Biol. 2012;22:1381–90. [PubMed: 22748321]

56. Wegener CS, Malerød L, Pedersen NM, Prodiga C, Bakke O, Stenmark H, et al. Ultrastructural characterization of giant endosomes induced by GTPase-deficient Rab5. Histochem Cell Biol. 2010;133:41–55. [PubMed: 19830447]

57. Schnatwinkel C, Christoforidis S, Lindsay MR, Uttenweiler-Joseph S, Wilm M, Parton RG, et al. The Rab5 effector Rabankyrin-5 regulates and coordinates different endocytic mechanisms. PLoS Biol. 2004;2:1363–80.

58. Kalin S, Hirschmann DT, Buser DP, Spiess M. Rabaptin5 is recruited to endosomes by Rab4 and Rabex5 to regulate endosome maturation. J Cell Sci. 2015;128:4126–37. [PubMed: 26430212]

59. Nag S, Rani S, Mahanty S, Bissig C, Arora P, Azevedo C, et al. Rab4A organizes endosomal domains for sorting cargo to lysosome-related organelles. J Cell Sci. 2018;131:jcs216226. [PubMed: 30154210]

60. Rains A, Bryant Y, Dorsett KA, Culver A, Egbaria J, Williams A, et al. Ypt4 and lvs1 regulate vacuolar size and function in Schizosaccharomyces pombe. Cell Logist; 2017;7:e1335270. [PubMed: 28944093]

61. Nazlamova L, Noble A, Schubert FR, McGeehan J, Myers F, Guille M, et al. A newly identified Rab-GDI paralogue has a role in neural development in amphibia. Gene. 2017;599:78–86. [PubMed: 27836664]

62. Bananis E, Murray JW, Stockert RJ, Satir P, Wolkoff AW. Regulation of early endocytic vesicle motility and fission in a reconstituted system. J Cell Sci. 2003;116:2749–61. [PubMed: 12759371]

63. Sorvina A, Shandala T, Brooks DA. Drosophila Pkaap regulates Rab4/Rab11-dependent traffic and Rab11 exocytosis of innate immune cargo. Biol Open. 2016;5:678–88. [PubMed: 27190105]

64. Perrin L, Lacas-Gervais S, Gilleron J, Ceppo F, Prodon F, Benmerah A, et al. Rab4b controls an early endosome sorting event by interacting with the gamma-subunit of the clathrin adaptor complex 1. J Cell Sci. 2014;127:258–258.

65. Myers EW, Miller W. Optimal alignments in linear space. Bioinformatics. 1988;4:11–7.

66. Hollestelle A, Nagel JHA, Smid M, Lam S, Elstrodt F, Wasielewski M, et al. Distinct gene mutation profiles among luminal-type and basal-type breast cancer cell lines. Breast Cancer Res Treat. 2010;121:53–64. [PubMed: 19593635]

67. Kim RK, Suh Y, Yoo KC, Cui YH, Kim H, Kim MJ, et al. Activation of KRAS promotes the mesenchymal features of Basal-type breast cancer. Exp Mol Med; 2015;47:e137–9. Available from: 10.1038/emm.2014.99 [PubMed: 25633745]

68. Sigismund S, Avanzato D, Lanzetti L. Emerging functions of the EGFR in cancer. Mol Oncol. 2018;12:3–20. [PubMed: 29124875]

69. Macé G, Miaczynska M, Zerial M, Nebreda AR. Phosphorylation of EEA1 by p38 MAP kinase regulates μ opioid receptor endocytosis. EMBO J. 2005;24:3235–46. [PubMed: 16138080]

70. Cavalli V, Corti M, Gruenberg J. Endocytosis and signaling cascades: A close encounter. FEBS Lett. 2001;498:190–6. [PubMed: 11412855]

71. Pinilla-Macua I, Grassart A, Duvvuri U, Watkins SC, Sorkin A. EGF receptor signaling, phosphorylation, ubiquitylation and endocytosis in tumors in vivo. Elife. 2017;6:1–25.

72. Collinet C, Stöter M, Bradshaw CR, Samusik N, Rink JC, Kenski D, et al. Systems survey of endocytosis by multiparametric image analysis. Nature. 2010;464:243–9. [PubMed: 20190736]

73. Wilson BJ, Allen JL, Caswell PT. Vesicle trafficking pathways that direct cell migration in 3D and in vivo. Traffic. 2018;1–11.

74. Linder S, Scita G. RABGTPases in MT1-MMP trafficking and cell invasion: Physiology versus pathology. Small GTPases. 2015;6:145–52. [PubMed: 26107110]

Implications statement

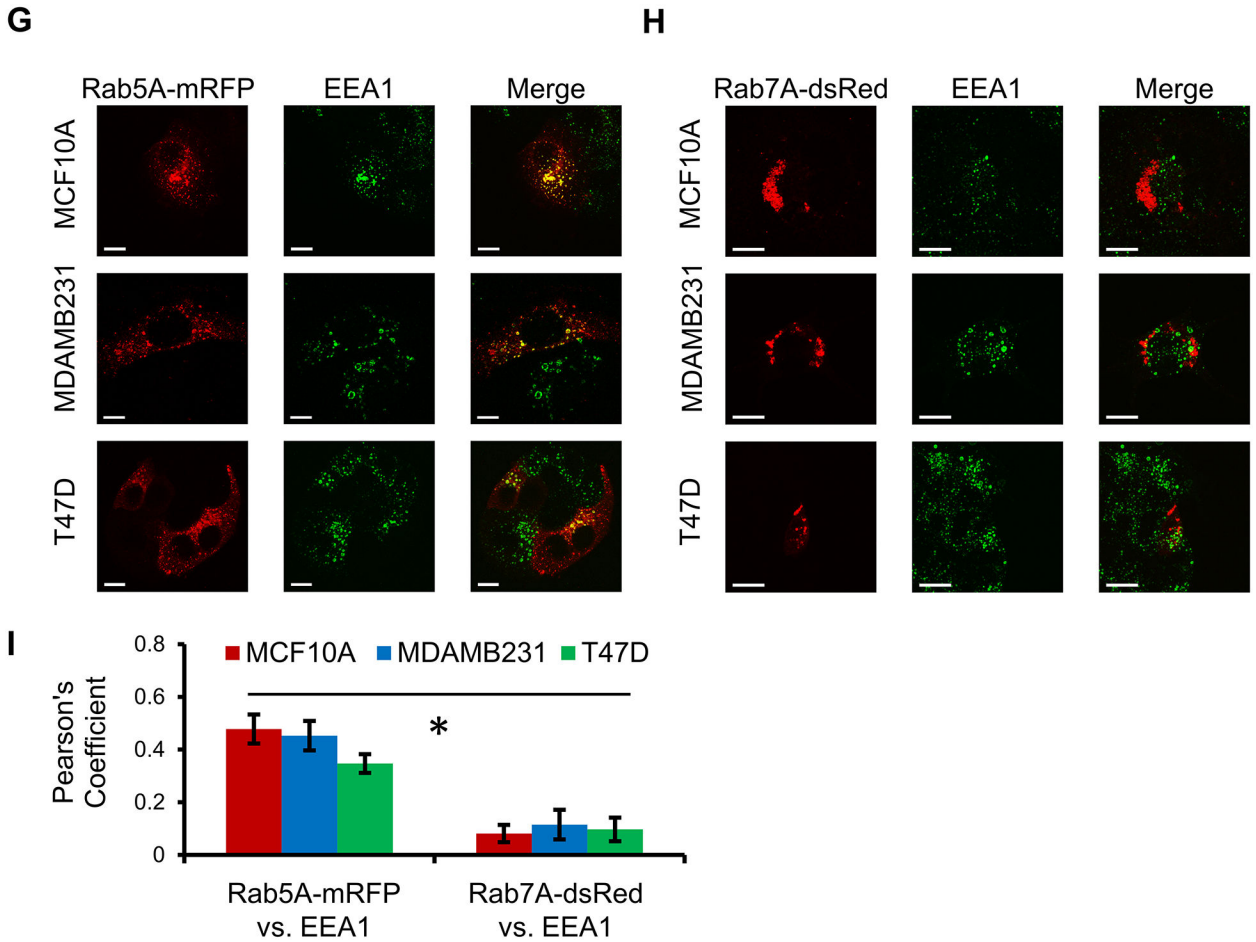Enlarged early endosomes play a Rab4-modulated role in regulation of EGFR activation in breast cancer cells

G

H

I
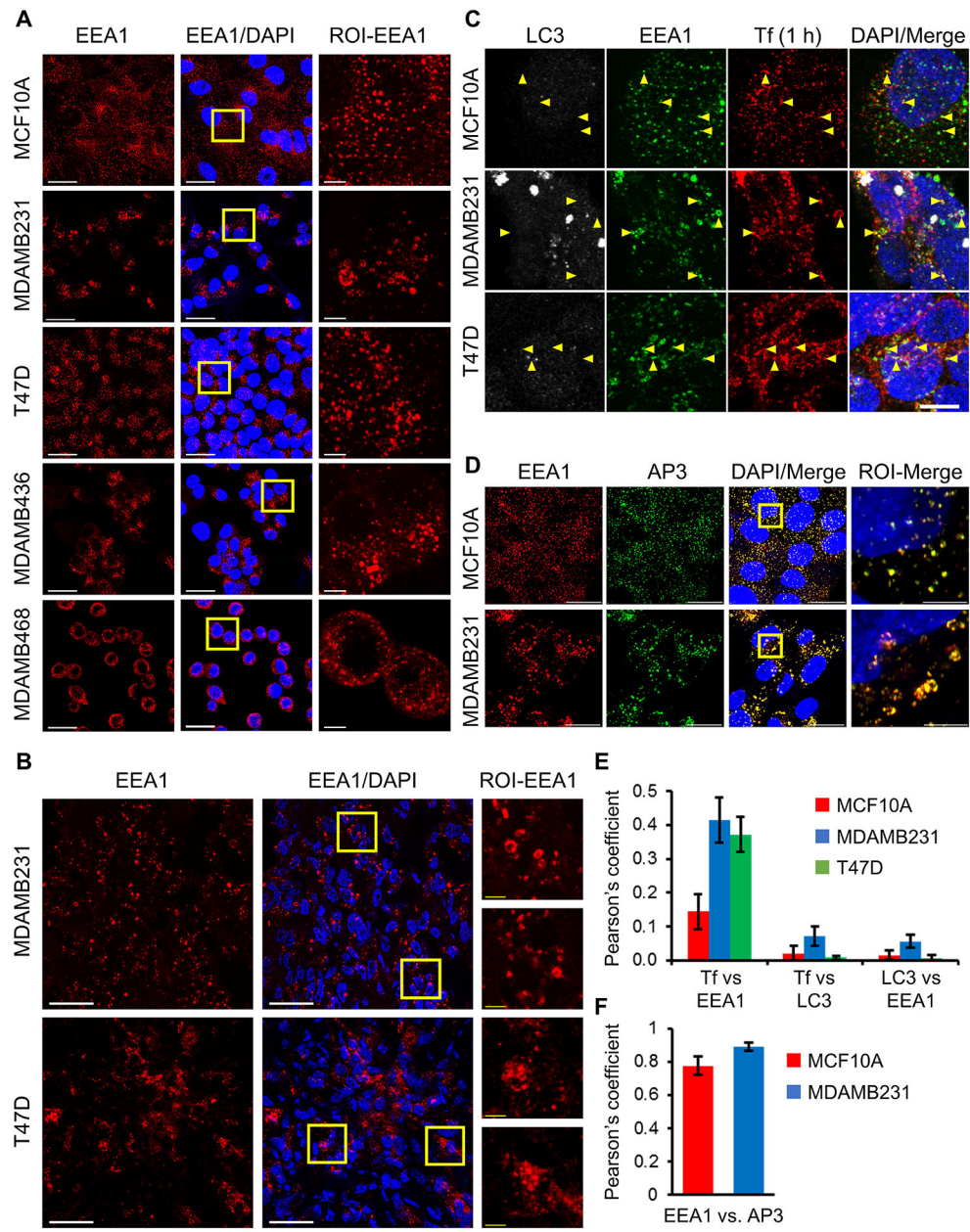
Figure 1. Early endosome morphology in human breast cancer cells and tumor xenografts.
(A) Non-cancerous MCF10A and breast cancer cell lines (MDAMB231, T47D, MDAMB436 and MDAMB468) were stained with anti-EEA1 and DAPI and imaged with confocal microscopy. **(B)** MDAMB231 and T47D tumor xenografts were fixed and stained with anti-EEA1 and DAPI. In **A-B**, ROI-EEA1 panels show high magnification of ROIs indicated in EEA1/DAPI panels as yellow squares. Left and middle panels, scale bar = 30μm; right panels, scale bar = 5μm. **(C)** MCF10A, MDAMB231 and T47D cells were internalized with fluorescently labeled Tf for 1 h at 37°C to identify early and recycling endocytic pathway. Upon fixation, cells were stained with anti-EEA1, anti-LC3 (autophagy marker) and DAPI. Arrowheads indicate discrete punctate structures that display Tf and EEA1, but no LC3 staining. Z-stack images were collected using confocal imaging. Scale bar = 10μm. Lower magnification images in Figure S3. **(D)** MCF10A and MDAMB231 cells were fixed and stained with anti-AP3 and anti-EEA1 and z-stacks were collected with Fast Airyscan microscopy. ROI-Merge panels show high magnification of ROIs indicated in Merge panel as yellow squares. EEA1, AP3 and Merge panels, scale bar = 20μm; ROI-Merge panels, scale bar = 5μm. In **C-D**, maximum intensity projection (MIP) images are shown with brightness and contrast settings adjusted for improved visualization. **(E)** Quantification of LC3, EEA1 and Tf colocalization from z-stack images in Figure 1C and **(F)** quantification of AP3 and EEA1 colocalization from z-stack images in Figure 1D, using

Pearson's coefficient in 3D volume (Coloc module, Imaris software). Statistics shown in Table S4. **(G-H)** Representative confocal MIPs of z-stack images of over-expressed wild-type Rab5A-mRFP **(G)** or Rab7A-dsRed **(H)** fusion constructs vs. EEA1 immunostaining. Scale bar = 10 μm. **(I)** Quantification of colocalization between Rab and EEA1 using Pearson's coefficient (in 3D volume). Statistical analysis is shown in Table S5. Error bars = 95% confidence interval.
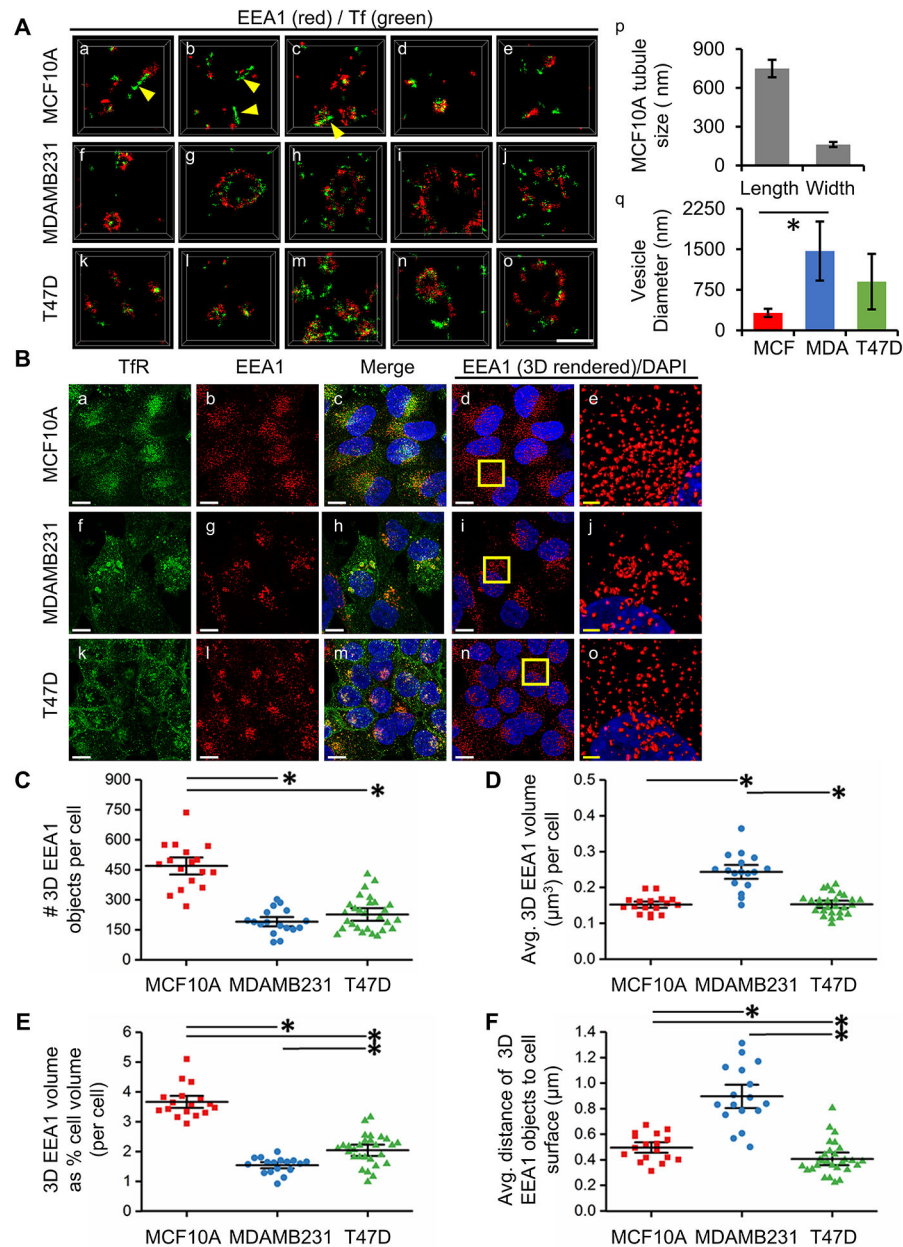
Figure 2. Super-resolution STORM and 3D whole-cell morphometric analysis of early endosomes in breast cancer cells.

(**A**) 3D *d*STORM super-resolution microscopy displays nanoscale resolution of enlarged EEA1 endosomes in breast cancer cells (MDAMB231 and T47D) and tubular Tf-positive structures in MCF10A cells. Cells were internalized with AF647-Tf for 1 h, fixed, stained with anti-EEA1 and subjected to 3D *d*STORM super-resolution microscopy. High magnification, several representative ROIs are shown for MCF10A (**a-e**), MDAMB231 (**f-j**), and T47D (**k-o**) cells with EEA1 (red) and Tf (green) staining; each ROI is shown in the XY perspective. White arrows point to tubular Tf structures found in MCF10A (**a-c**). Scale bar = 1000 nm. *d*STORM measurements of tubular (**p**) and vesicular structures (**q**). Statistics in Table S6. 3D rotational views are shown in Videos S1–2. Lower magnification images

displaying z-depth pseudo-coloring are shown in Figure S5. **(B)** Representative images of MCF10A **(a-c)**, MDAMB231 **(f-h)**, and T47D **(k-m)** cells are shown as MIP from Fast Airyscan z-stacks displaying anti-TfR (green), anti-EEA1 (red) and DAPI (blue) staining; MIP images are shown with brightness and contrast settings adjusted for improved visualization. Then, z-stack images of MCF10A **(d-e)**, MDAMB231 **(i-j)** and T47D **(n-o)** were subjected to Imaris 3D rendering "surface" module to generate 3D rendered EEA1 objects. Imaris 3D rendering schematic is shown in Figure S6. Right panels (**e, j, o**) show high magnification of ROIs indicated in **d, i, n** panels as yellow squares, respectively. White scale bar = 10 μm, yellow scale bar on ROI panels = 2 μm. **(C-F)** Whole-cell morphometric analysis includes number of 3D-rendered EEA1 objects per cell **(C)**, average volume (μm^3) of 3D EEA1 objects per cell **(D)**, total 3D EEA1 object volume as percent of cell volume per cell **(E)** and average 3D Euclidean distance of 3D EEA1 objects to cell surface (μm) **(F)**; n= 17–28 cells; statistical data shown in Table S7. Additional quantification in Figure S7. Statistical significance (p<0.05) is indicated with asterisk. Error bars = 95% confidence interval.
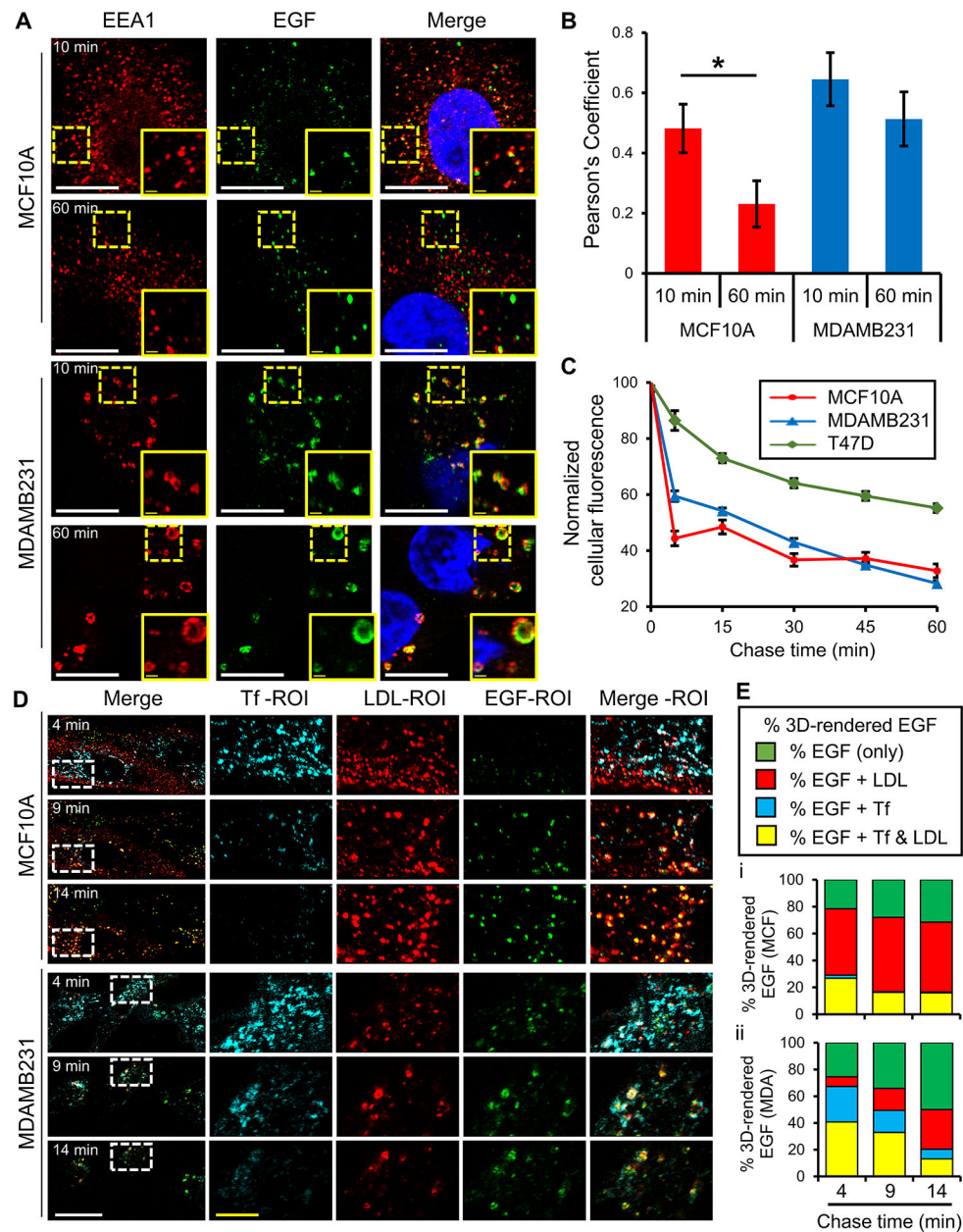
Figure 3. Alterations in endosome maturation and cargo sorting dynamics of LDL, EGF and Tf.
(A-B) EGF-positive endosomes have delayed maturation in MDAMB231 compared to
MCF10A. Cells were pulsed with AF488-EGF (green) for 10 min, and then fixed or chased
for an additional 50 min prior to immunostaining with anti-EEA1 (red). (**A**) Representative
MIP fast Airyscan images are shown, with an ROI selected from each image (dotted yellow
squares) shown in higher magnification inset (solid yellow squares). White scale bar = 10
μm, yellow scale bar (inset) = 1 μm. (**B**) Colocalization between EEA1 and EGF, shown as
Pearson's coefficient collected from z-stacks at each time point (Coloc module, Imaris).
Statistical significance (p<0.05) is shown with asterisk; statistics are shown in Table S8. (**C**)
Tf recycling behavior is similar in MCF10A and MDAMB231 cells. Data from 96-well plate
reader Tf recycling assay was pooled from 5 separate experiments, with a minimum of 200
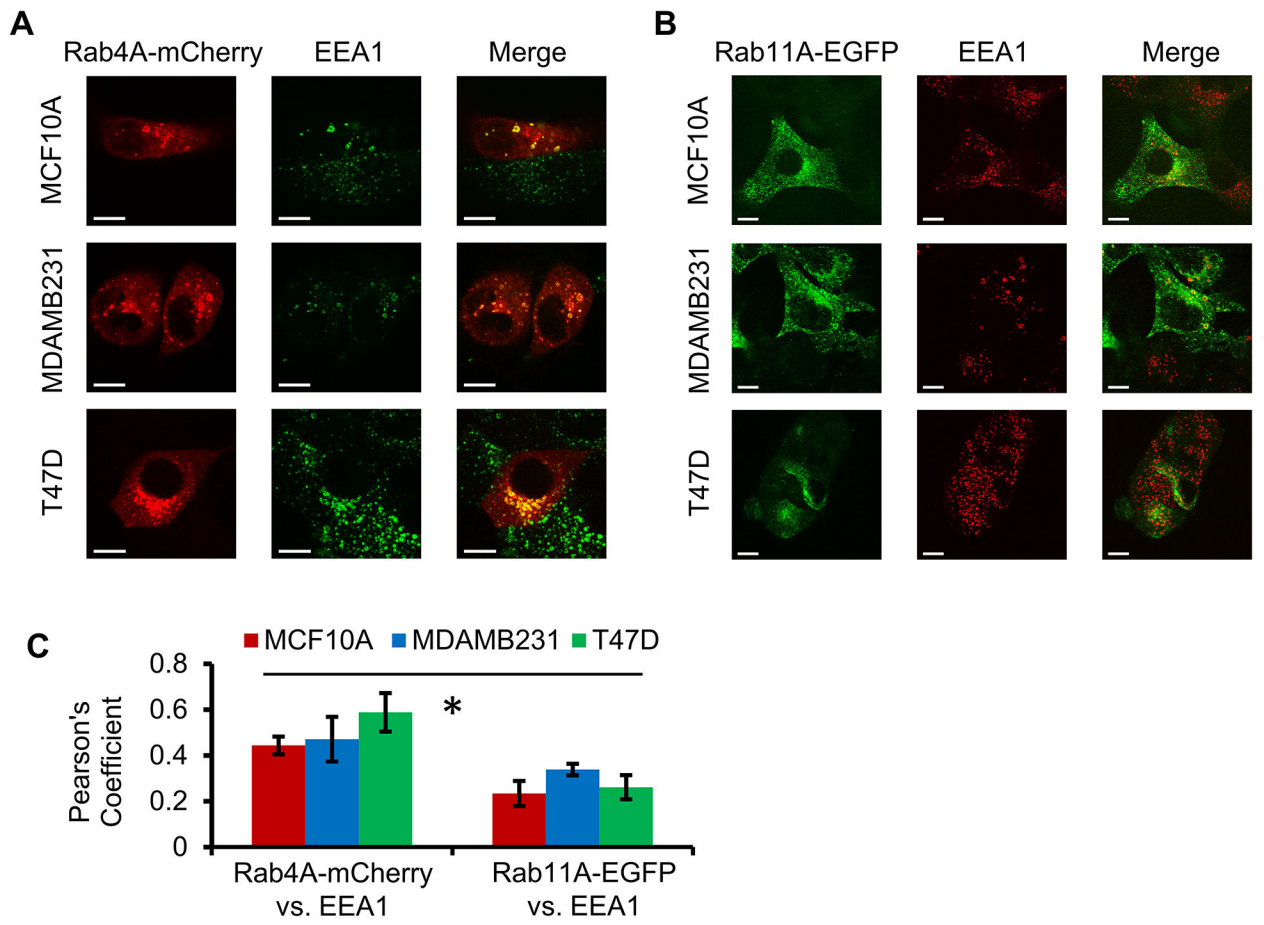
reads per time-point and cell line. Statistical analysis is shown in Table S8. **(D-E)** Live-cell imaging of differently fluorescently labeled EGF, Tf and LDL ligands indicates MCF10A have more segregated endocytic compartments compared to MDAMB231. Cells were pulsed for 2 min with AF488-EGF, DiI-LDL and AF647-Tf, followed by live-cell Fast Airyscan z-stack imaging starting 4 min post-pulse. Z-stacks were collected every 60 s for 15 min. Live-cell time-lapse is shown in Video S3. **(D)** Representative MIP images for MCF10A and MDAMB231 cells are shown at 4, 9 and 14 min. ROIs (dotted white rectangles in Merge panels) are shown in higher magnification for Tf-ROI (cyan), LDL-ROI (red), EGF-ROI (green) and Merge-ROI (right) panels. MIP images are shown with brightness and contrast settings adjusted for improved visualization. White scale bar = 20 μm, yellow scale bar = 5 μm. **(E)** Cumulative bar charts for % 3D-rendered EGF objects at 4, 9 and 14 min are shown for MCF10A (panel **i**) and MDAMB231 (panel **ii**). Green displays % of 3D EGF objects containing only AF488-EGF intensity signal, red displays % of 3D EGF objects containing both AF488-EGF and DiI-LDL intensity signals, blue displays % of 3D EGF objects containing AF488-EGF and AF647-Tf intensity signals, and yellow displays % of 3D EGF objects containing all AF488-EGF, DiI-LDL and AF647-Tf intensity signals. Statistical analysis is shown in Table S11. Receptor expression levels are shown in Figure S8, and additional quantification of live-cell trafficking in Figure S9. Error bars = 95% confidence interval.
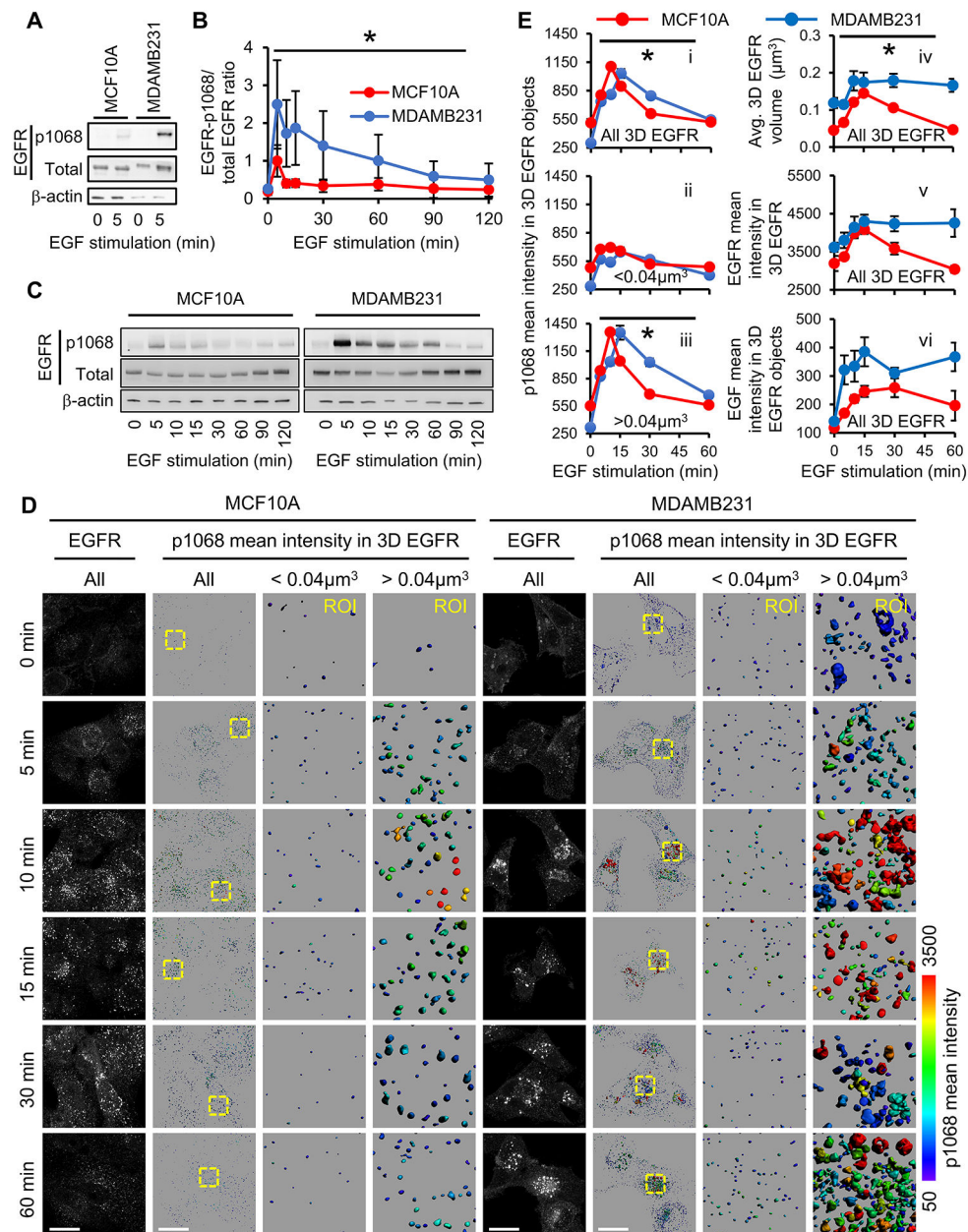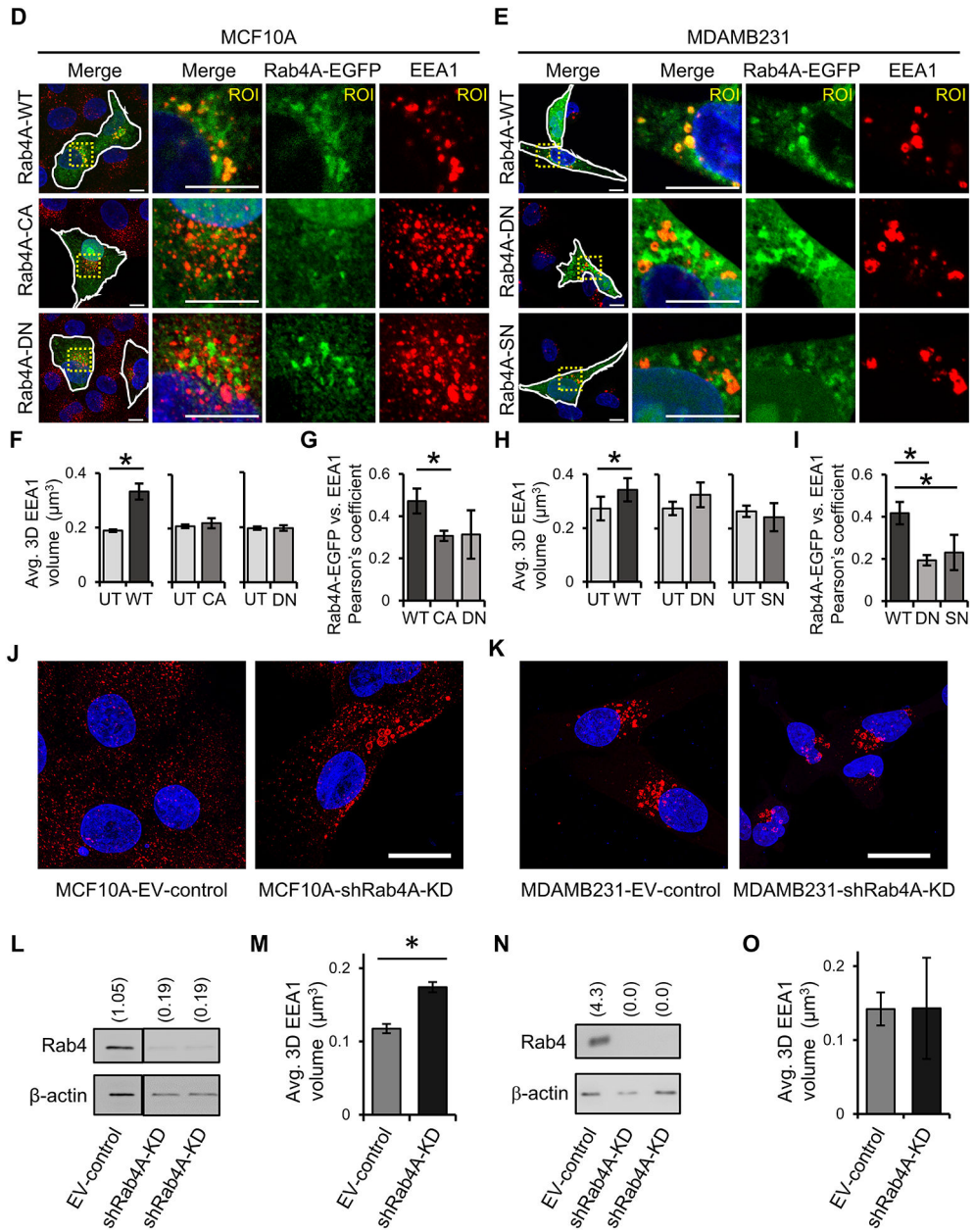
Figure 4. EGF-mediated EGFR-p1068 activation is prolonged in enlarged endocytic vesicles of MDAMB231 cells.

(A-D) MCF10A and MDAMB231 cells were stimulated with unlabeled EGF for 0 or 5 min and chased for different periods of time. Cells were then lysed for immunoblotting analysis with antibodies against EGFR-p1068, total EGFR and β-actin. **(A)** Immunoblotting of MCF10A and MDAMB231 lysates at 0 and 5 min of EGF stimulation. **(B-C)** Quantification and representative western blots for EGFR-p1068 / total EGFR ratio. Quantification and representative western blots for pAKT/ total AKT ratio and pERK/ total ERK ratio are shown in Figure S10. Each protein blot signal was normalized to β-actin signal followed by ratio and normalization to maximum response of MCF10A within each independent experiment, n=3–5. Statistical analysis available in Table S12. **(D-E)** MCF10A and

MDAMB231 cells were stimulated with AF488-EGF for 0 or 5 min and chased for different periods of time, fixed and stained with anti-EGFR-p1068, anti-EGFR and DAPI. Z-stacks were collected using Fast Airyscan microscopy and subjected to 3D rendering of EGFR objects using Imaris 3D rendering "surface" module. 3D EGFR objects were then split by size as outlined in Figure S11. **(D)** MIP grayscale images are shown for total EGFR raw images (**All, EGFR** panels). The EGFR-p1068, EGF and DAPI channel are shown in Figure S12. Total 3D EGFR objects displaying EGFR-p1068 mean intensity are shown at same magnification (**All, p1068** panels); scale bar = 20 μm. **ROI** panels show 3D total EGFR displaying EGFR-p1068 signal split by object volume below or above $0.04\mu m^3$. The pseudo-color range is based on the intensity mean of the EGFR-p1068 channel (range 50–3500). High magnification ROI is shown in insert of 10 μm x10 μm. **(E)** Quantification of EGFR-p1068 intensity levels inside 3D EGFR objects is shown for all objects (**All 3D EGFR - i** graphs) or split by object volume (**$<0.04\mu m^3$- ii** graphs or **$>0.04\mu m^3$- iii** graphs). The distribution of 3D EGFR by size is in Figure S12B. Average of 3D EGFR object volume is shown for all structures (**iv** graphs) and mean intensity of EGFR (**v** graphs) or EGF (**vi** graphs) within the 3D EGFR objects. MDAMB231 (blue) and MCF10A (red) data is shown. Detailed statistical analysis is shown in Table S13. Error bars = 95% confidence interval. Asterisks indicate statistical significance ($p < 0.05$).

A Rab4A-mCherry EEA1 Merge

MCF10A
MDAMB231
T47D

B Rab11A-EGFP EEA1 Merge

MCF10A
MDAMB231
T47D

C
MCF10A ■ MDAMB231 ■ T47D

Pearson's Coefficient

Rab4A-mCherry vs. EEA1   Rab11A-EGFP vs. EEA1

Figure 5. Rab4 modulates endosomal size.

(A-B) Representative confocal MIPs of z-stack images Rab4A-mCherry **(A)** and Rab11A-eGFP **(B)** fusion constructs vs. EEA1 immunostaining. Scale bar = 10 μm. **(C)** Quantification of colocalization between Rab and EEA1 stainings using Pearson's coefficient (in 3D volume). Statistical analysis is shown in Table S5**. (D-I)** Wild-type Rab4A-WT, constitutively active Rab4A-CA (Q67L) or dominant negative Rab4A-DN (N121I) eGFP or dominant negative Rab4A-S22N mCherry fluorescent protein constructs were expressed in MCF10A or MDAMB231 cells. **(D and E)** Representative MIP visualization of Fast Airyscan z-stacks are shown for Rab4A (WT, CA, DN, SN; green), EEA1 (red) and DAPI (blue). Merge left panels display transfected cells outlined in white. ROI (dotted yellow square) in Merge left panels is shown at higher magnification in three

right ROI (yellow) panels. Scale bar = 10 μm. (**F and H**) Quantification of 3D EEA1 object volume (μm^3) from transfected (WT, CA, DN or SN) and untransfected (UT; not outlined) cells in MCF10A (**F**) or MDAMB231 (**H**). Statistical analysis is shown in Table S14; n=1820–17101 or n=881–7797 3D EEA1 objects pooled from multiple z-stacks images of representative experiments for MCF10A and MDAMB231 respectively. (**G and I**) Colocalization of Rab4-WT, Rab4-CA, Rab4-DN, Rab4-SN vs. EEA1 shown as Pearson's coefficient (in 3D volume) in MCF10A (**G**) and MDAMB231(**I**). Statistical analysis is shown in Table S15. (**J-O**) MCF10A and MDAMB231 cells were subjected to shRNA Rab4A (shRab4A-KD) or empty vector (EV) with GFP reporter lentiviral infection. (**J and K**) Representative MIP images from Fast Airyscan z-stacks for EV-control (**left**) and Rab4A-shRNA (**right**) cells immunostained with anti-EEA1 and DAPI. Immunoblotting analysis of anti-Rab4 and anti-β-actin in whole-cell lysates for MCF10A (**L**) and MDAMB231 (**N**). Quantification of 3D EEA1 object volume (μm^3) in EV-control and Rab4A-shRNA cells for MCF10A (**M**) and MDAMB231 (**O**). Statistical analysis is shown in Table S16. Statistical significance ($p<0.05$) is indicated with asterisk. Error bar = 95% confidence interval.
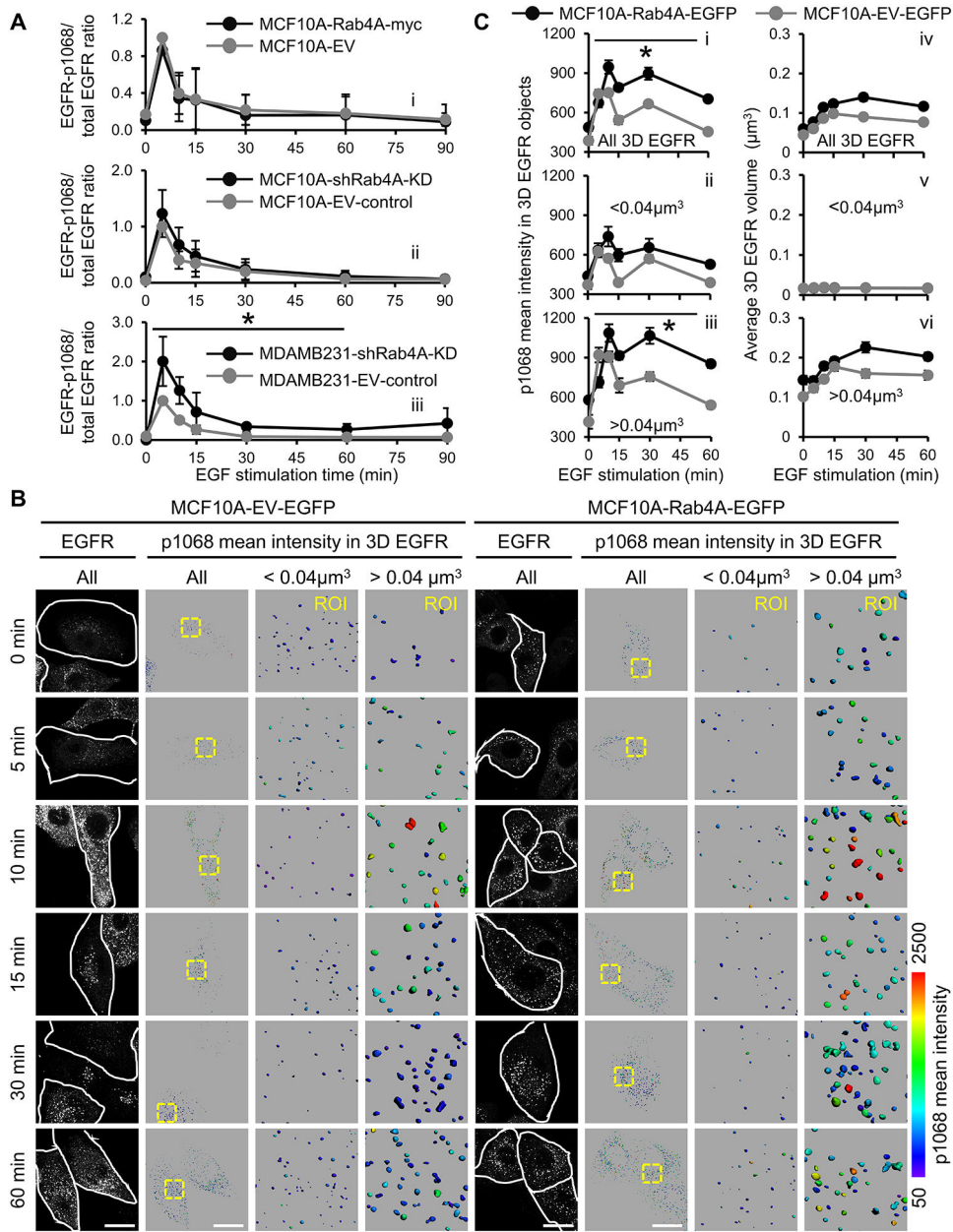
Figure 6. Complex Rab4A modulation of EGFR activation in enlarged EEs.
(A) Cells were stimulated with unlabeled EGF for 0 or 5 min, and either fixed immediately or chased for different periods of time. Whole cell lysates were used for immunoblotting analysis with antibodies against EGFR-p1068 and total EGFR and β-actin. Quantitation of EGFR-p1068/ total EGFR for MCF10A over-expressing empty vector (EV) or Rab4A-myc constructs (**Graph i**), EV-control and Rab4-shRNA MCF10A cells (**Graph ii**) or EV-control and Rab4-shRNA MDAMB231 cells (**Graph iii**). Quantification and representative western blots for EGFR-p1068 / total EGFR ratio, pAKT/ total AKT ratio and pERK/ total ERK ratio are shown in Figure S14 and 15. Each protein blot signal was normalized to β-actin signal followed by ratio and normalization to EV-control within each independent experiment; n=3. Statistical analysis available in Table S18. **(B)** MCF10A cells transfected

with GFP-EV control or wild-type Rab4A-EGFP were stimulated with unlabeled EGF for 0 or 5 min and either fixed immediately or chased for different periods of time. Cells were immunostained with anti-EGFR-p1068 and anti-EGFR. Z-stacks were collected using Fast Airyscan microscopy and subjected to 3D rendering using Imaris software. Fluorescence intensity levels were calculated in 3D EGRF objects split by endosomal size as described in Figure 4D–E and Figure S11. Only transfected cells (white outline) were analyzed. MCF10A-EV-EGFP and MCF10A-Rab4A-EGFP cells are shown, at same magnification, as total EGFR raw grayscale images (**All, left** panel) and 3D rendered EGFR objects displaying p1068 mean intensity (**All, right** panel). Scale bar = 20 μm. An ROI (yellow dotted square) is shown at higher magnification in the two ROI right panels. 3D EGFR objects are shown split by object volume (**<0.04 μm^3** and **>0.04 μm^3** panels). Pseudo-color of 3D EGFR objects is based on the intensity mean of the EGFR-p1068 channel (50 – 2500 range). High magnification ROI is shown in insert of 10×10μm. The GFP and DAPI channel are shown in Figure S16A. **(C)** Quantification of EGFR-p1068 intensity levels inside 3D EGFR structures is shown in all 3D EGFR objects (Graph **i**) or split by object volume below or above 0.04μm^3 (Graph **ii and iii**, respectively). Quantification of average 3D EGFR volume (μm^3), shown for all 3D EGFR objects (Graph **iv**), or split by object volume below or above 0.04μm^3 (Graph **v and vi**, respectively). Statistical analysis is shown in Table S19. The distribution of 3D EGFR endosomal populations are shown in Figure S16B. Error bars = 95% confidence interval. Asterisks indicate statistical significance ($p< 0.05$).